

**AN INVESTIGATION OF THE
METROLOGICAL & SPECTROSCOPIC CAPABILITIES
OF AN AMBIENT STM**

A thesis for the Degree of M.Sc.

Presented to Dublin City University

by

Sean Hearne, B.Sc.

School of Physical Sciences

Dublin City University

Research Supervisor

Dr. Greg Hughes.

September 1997

Declaration.

I hereby certify that this material , which I now submit for assessment on the program of study leading to the award of M.Sc. is entirely my own work and has not been taken from the work of others save and to the extent of such work has been cited and acknowledged within the text of my work.

Signed : Seán Gleasne
Candidate

Date : 20/1/98

Acknowledgements.

I would firstly like to thank Dr Greg Hughes for all his help and endless insights into the world of surface science over the last couple of years I am also grateful to Dr Paul Hetherington and Howard McQuoid at The National Metrology Lab , Forbairt for their guidance in all matters metrological Rosalba Rizza, UCD for the gold samples Special thanks to Al Devine for his help with the numerous diagrams that were scanned in I would also like to thank Dr Tony Caffola and my other colleagues Philip, Terri, Paul, Dr Justin and Elish for their help throughout in all things surface related Also Neil for his constant pestering over breakfast The Chemistry boys and girls Aidan, Paud, Colm, Penny and Anto Last but not least my family who are still waiting for the repayments to start and Rachael who was very understanding about the lack of time I had to go shopping with her

Abstract

The first part of this thesis investigates the establishment of a calibration procedure for the Nanoscope II Scanning Tunnelling Microscope (STM) based on the use of calibration standards, which have been certified by the National Institute of Standards and Technology (NIST). Two measurement techniques are compared. One involves taking a fast Fourier transform (fft) of a surface profile, the resulting measurement corresponds to the period of the optimum frequency of the fft spectrum. In the other method the surface profile is differentiated and the measurement corresponds to separation of consecutive peaks on the differential curve.

The second part focused on Scanning Tunnelling Spectroscopy (STS) measurements of the Au(111) surface in air and liquid environments. A characteristic I-V curve was obtained for the Au(111) surface using current-voltage (I-V) spectroscopy. The apparent tunnelling barrier height was calculated from current-distance (I-S) spectroscopy. For the Au(111) surface imaged in Decalm a value of 1.4 eV was calculated for the apparent barrier height, while for the same surface in air a value of 1.0 eV was calculated.

The final part of this thesis involved a study of the native oxide and sulphur passivated InP(100) surfaces and preliminary measurements on Germanium surfaces. X-ray photoemission spectroscopy (XPS) was used to determine the chemical composition of the InP surfaces. STM images of the native oxides of InP(100) surfaces were found to have a root mean square (rms) roughness greater than that of the sulphur passivated surface. I-V spectroscopy of both the native oxide and sulphur passivated InP(100) displayed characteristics similar to those observed for corresponding treatments to the GaAs surface. I-S spectroscopy of the native oxide on InP(100) gave an apparent barrier height of 0.3 eV, while for the sulphur passivated InP(100) surface the value was 0.05 eV. The very low apparent barrier height on the passivated surface was attributed to the effects of tip-induced band bending. Further STS studies of the native oxides on Ge(111) surface and hydrogen passivation of that surface display the same trends as observed on InP(100).

Table of Contents

ABSTRACT	1
CHAPTER 1 : THEORY OF THE SCANNING TUNNELLING MICROSCOPE AND TUNNELLING SPECTROSCOPY.	2
1 1 THE TUNNELLING EFFECT	2
1 2 THE SCANNING TUNNELLING MICROSCOPE	4
1 3 SCANNING TUNNELLING SPECTROSCOPY	6
1 3 1 <i>Current-Voltage(I-V) spectroscopy</i>	6
1 3 2 <i>Current-Distance(I-S) spectroscopy</i>	10
References	11
CHAPTER 2 · EXPERIMENTAL SYSTEMS AND TECHNIQUES.	12
2 1 THE NANOSCOPE II AIR STM	12
2 1 1 <i>Instrumentation</i>	12
2 1 2 <i>Image Acquisition</i>	14
2 1 3 <i>Calibration considerations</i>	14
2 1 4 <i>Acquisition of Spectroscopic data</i>	15
2 2 X-RAY PHOTOEMISSION SPECTROSCOPY	15
CHAPTER 3 : CALIBRATION OF THE STM	17
3 1 INTRODUCTION	17
3 2 INFLUENCE OF THE TIP ON THE MEASUREMENT PROCESS	17
3 3 MOTIVATION FOR DEVELOPMENT OF PROFILE DIFFERENTIATION	22
3 4 SURFACE TOPOGRAPHY STANDARDS	24
3 5 PROGRAM USED TO OBTAIN MEASURED VALUES	25
3 6 EXPERIMENTAL CONDITIONS	26
3 7 RESULTS	27
3 7 1 <i>Precision of measurements</i>	28
3 7 2 <i>Accuracy of Measurements</i>	30
3 7 3 <i>Instrument Confidence</i>	34
3 8 CONCLUSIONS	37
References	38
CHAPTER 4 . SCANNING TUNNELLING SPECTROSCOPY OF GOLD IN AIR.	39
4 1 INTRODUCTION	39
4 2 REVIEW OF LITERATURE ON APPARENT BARRIER HEIGHT	39
4 3 PREPARATION OF SAMPLES USED	42
4 4 CALIBRATION OF SMALL AREA SCAN HEAD	42
4 5 CALCULATION OF THE APPARENT BARRIER HEIGHT FROM EXPERIMENTAL DATA	44
4 6 SCANNING TUNNELLING SPECTROSCOPY OF THE Au(111) SURFACE	46
4 6 1 <i>I-V spectroscopy</i>	46
4 6 2 <i>I-S spectroscopy</i>	46
4 7 CONCLUSIONS	52
References	53
CHAPTER 5 : STM/S OF SULPHUR PASSIVATED INP.	54
5 1 INTRODUCTION	54
5 2 PASSIVATION OF SEMICONDUCTOR SURFACES	54
5 3 LITERATURE REVIEW	57
5 4 XPS STUDY OF INP	59
5 5 SURFACE ROUGHNESS	60
5 6 I-V SPECTROSCOPY	61
5 7 I-S SPECTROSCOPY	65
5 8 CONCLUSION	66
References	67

CHAPTER 6 : STM/S OF GERMANIUM.....	69
6 1 INTRODUCTION	69
6 2 EXPERIMENTAL	69
6 3 STM IMAGES OF GE	70
6 4 SCANNING TUNNELLING SPECTROSCOPY OF GE	71
6 4 1 <i>I-V Spectroscopy</i>	71
6 4 2 <i>I-S Spectroscopy</i>	74
6 5 CONCLUSIONS	75
References	76
CHAPTER 7 . CONCLUSIONS.	78
7 1 SUMMARY OF METROLOGICAL WORK	78
7 2 CONCLUSIONS OF STS WORK	79
7 3 SUGGESTIONS FOR FUTURE RESEARCH	80
References	80
APPENDIX A RMS ROUGHNESS CALCULATION	1
APPENDIX B REFEREED PUBLICATIONS	1

List of Figures.

Figure caption	Page Number
CHAPTER 1	
Fig 1 1 (a) A simple one dimensional rectangular barrier of height, V_0 (b) The probability density function, P for typical (rectangular) barrier penetration	2
Fig 1 2 Schematic energy level diagram of metal-vacuum-metal system at (a) thermodynamic equilibrium and (b) with metal 2 positively biased	3
Fig 1 3 Schematic of the STM experiment (after Ref [1])	5
Fig 1 4 Expected I-V plot for metal-vacuum-metal system	7
Fig 1.5 Energy level diagrams for a metal-insulator-semiconductor system at (a) thermodynamic equilibrium, (b) low negative bias and (c) high negative bias	8
Fig 1 6 Expected I-V plots for (a) intrinsic, (b) extrinsic semiconductor	9
CHAPTER 2	
Fig 2.1 Picture of Nanoscope II air STM scanner	12
Fig 2 2 Schematic diagram of the Nanoscope II air STM	13
Fig 2 3 Schematic of Clam 100 from VG Scientific	16
CHAPTER 3	
Fig 3 1 Scan line produced by a blunt probe encountering a sudden step (after Ref [5])	18
Fig 3 2. $(160\text{nm})^2$ STM image of a cleavage step on an Au coated NaCl crystal, with the vertical range shown on the left in nm	19
Fig 3 3 Estimated tip shape from cleavage steps of the Au coated single crystalline NaCl Included are parabolic curve fits of tip shape	20
Fig 3 4(a) Sample profiles taken from STM images of 3,10 and 20 μm pitch calibration grids	21
Fig 3 4(b) Actual shape of step from manufacturers specifications	21
Fig 3.5(a) Simulated step profile of 3 μm pitch grid	22
Fig 3 5(b) Comparison of simulated profile of 3 μm pitch grid and profile taken from $(20 \mu\text{m})^2$ scan of 3 μm pitch grid	23
Fig 3 6 Contour plots of calibration grids with (a) unsuitable and (b) suitable reference lines	26
Fig 3 7 Sample profile from $(40\text{m}\mu)^2$ scan of 10 μm pitch grid(top) and its derivative(bottom)	27
Fig 3 8 Comparison of profiles taken with W and PtIr tips taken from $(20\mu\text{m})^2$ scan of 3 μm pitch grid	29
Fig 3 9 (a)Comparison of pitch measurements in the x-directions using a Pt-Ir tip taken via the profile differentiation and FFT methods for various scan areas Included are specified pitch value(solid red lines) and tolerances(dashed red lines) (b)and(c) are expanded plots for the 10 μm and 3 μm pitch data, respectively	33
Fig 3 10 (a)Pitch measurements taken (profile differentiation) m x and y-directions from various scan areas using both Pt-Ir and W tips Included are specified pitch value(solid red lines) and tolerances(dashed red lines) (b)and(c) are expanded plots for the 10 μm and 3 μm pitch data respectively	35

CHAPTER 4

<i>Fig 4.1</i> The variation in apparent barrier height with tip-sample separation (after Ref. [9]). Φ is the average workfunction of the sample, ϕ_A is the apparent barrier height.	40
<i>Fig 4.2.</i> $(60.75 \text{ nm})^2$ scan of HOPG	43
<i>Fig 4.3.</i> 82x50 nm STM image of atomic steps on the Au(111) surface.	43
<i>Fig 4.4.</i> Profiles taken of stepped area of Fig 4.3. Measurements of the step heights are also shown.	44
<i>Fig 4.5.</i> I-S spectroscopic plot of the Au(111) surface imaged in Air, at various tunnelling currents, I_t	45
<i>Fig 4.6.</i> Typical I-V curves for Au(111) surfaces.	46
<i>Fig 4.7.</i> I-S spectroscopic plot of the Au(111) surface imaged in Decalin.	47
<i>Fig 4.8.</i> Variation in apparent barrier height with applied bias (V_b)	48
<i>Fig 4.9.</i> Variation in barrier height with applied bias for Au(111) prepared on Si and Mica substrates. Samples imaged in air.	49
<i>Fig 4.10.</i> Sketch of how fixed polarisation of the tunnel gap affects tunnelling at positive and negative sample bias.	49
<i>Fig 4.11.</i> Variation in apparent barrier height with surface roughness for various Au surfaces.	50
<i>Fig 4.12</i> Sketch showing effect of (a) smooth and (b) rough surface can have on I-S spectroscopy.	51

CHAPTER 5

<i>Fig 5.1</i> Surface state induced band bending in a semiconductor.	55
<i>Fig 5.2</i> Formation of a Schottky barrier between a metal and an n-type semiconductor (a) metal and semiconductor separated (b) Metal and semiconductor in contact.	56
<i>Fig 5.3.</i> Survey XPS spectra of native oxide and sulphur treated InP, showing the drop in intensity of the Carbon and Oxygen signals prior to sulphur treatment.	59
<i>Fig 5.4.</i> XPS spectra of the Phosphorus 2p peak for the native oxide and sulphur treated InP samples.	60
<i>Fig 5.5.</i> 3-D plots of STM images of the native oxide and sulphur passivated InP surface.	61
<i>Fig 5.6.</i> I-V spectroscopic plots for the native oxide and sulphur passivated InP.	62
<i>Fig 5.7.</i> Variation in subsequent I-V plots taken on sulphur passivated InP.	63
<i>Fig 5.8.</i> STM images of sulphur passivated InP (a) before I-V spectroscopy, after I-V spectroscopy and (c) after second set of I-V spectroscopic measurements after tip had been moved to top right of previous image.	64
<i>Fig 5.9.</i> I-S curves of the Au(111), Native oxide of InP and S passivated InP.	65

CHAPTER 6

<i>Fig 6.1.</i> Surfaces plots of STM images of (a) the native oxide and (b) HF etched Ge(111) surfaces. Vertical scale is in nm.	71
<i>Fig 6.2.</i> I-V spectroscopic plots for the native oxide and HF etched Ge(111) surface	72
<i>Fig 6.3.</i> I-V plots in log form for the native oxide and HF etched Ge(111) surfaces.	73
<i>Fig 6.4.</i> Shows damage induced by (a) imaging the H:Si(111) surface at +3.5V (after Ref. [14]) and (b) performing I-V spectroscopy on the HF etched Ge(111) surface.	74
<i>Fig 6.5.</i> Variation in measured apparent barrier height for the native oxide and HF etched Ge(111) surface at different setpoint voltages.	75

Chapter 1 : Theory of the Scanning Tunnelling Microscope and Tunnelling Spectroscopy

1.1 The Tunnelling Effect

The Tunnelling effect originates from the wavelike properties of particles in quantum mechanics. When a particle of energy E , is incident upon a barrier with a potential energy, V_0 , where V_0 is greater than E , there is a finite probability that the particle may traverse the forbidden region and appear at the other side of the barrier (see Fig 1.1). Classically, such a particle would have zero probability of penetrating the potential barrier. However, in quantum mechanics the probability of a particle of energy E , penetrating a particular potential energy barrier can be approximated by solving the 1-dimensional time independent Schrodinger wave equation

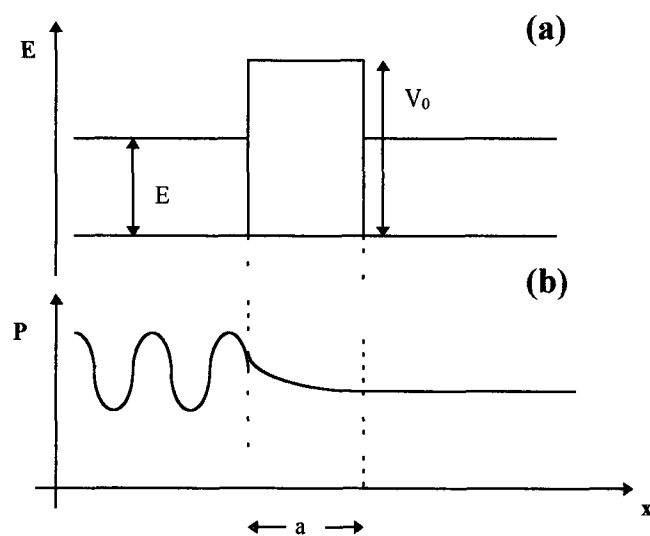


Fig 1.1 (a) A simple one dimensional rectangular barrier of height, V_0 (b) The probability density function, P for typical (rectangular) barrier penetration

Solving the 1-dimensional time independent Schrodinger wave equation yields solutions which show that the finite probability of transmission, T , of the particle through the barrier of width a , can be described by the expression,

$$|T|^2 \propto \exp^{-ka} \quad \text{eqn (1.1)}$$

where $\kappa^2 = \frac{2m}{\hbar^2}(V_0 - E)$ eqn (1.2)

m is the mass of an electron and $\hbar = h/2\pi$, where h is Planck's constant.

From these equations it is clear that the transmission of the particle through the barrier (and hence the tunnelling probability) is very sensitive because of its exponential dependence to both the barrier thickness, a , and the energy of the particle relative to that of the barrier, $(V_0 - E)$

To observe the tunnel effect in practice consider two metals separated by a vacuum gap of width, a . In Fig 1.2(a) we see an energy level diagram of the system. The energy levels are considered occupied to the Fermi levels and the energy states above the Fermi levels are for the most part considered empty (a valid assumption at room temperature)

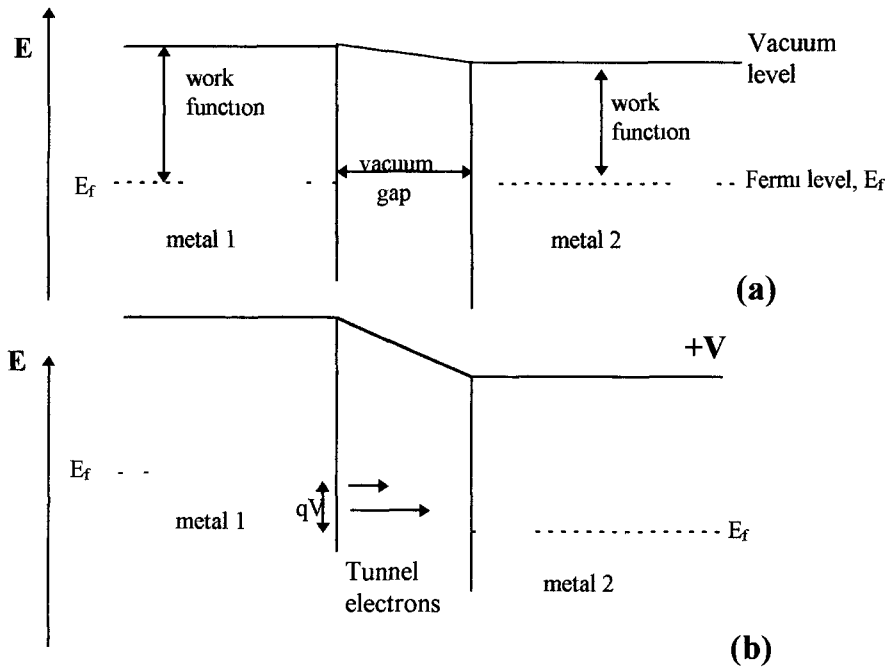


Fig 1.2 Schematic energy level diagram of metal-vacuum-metal system at (a) thermodynamic equilibrium and (b) with metal 2 positively biased

With no biasing of either of the metals no net tunnelling occurs because the Fermi levels will be the same, thus any electrons tunnelling through the vacuum region will not have free energy levels which they can tunnel into

Biasing one of the metals with respect to the other has the effect of shifting the energy levels relative to one another, see Fig 1 2(b) A bias voltage of magnitude, V will shift the energy levels by a factor qV , where q is the charge of an electron As we see in the diagram electrons with energies between E_f and $E_f - qV$ in the negatively biased electrode tunnel into the empty states above the Fermi level of the positively biased electrode

From the diagrams we see that the height of barrier (referred to as V_0 in Fig 1 1(a)) is equal to the work function of the metal It was pointed out that the transmission of electrons through the barrier was dependant on $V_0 - E$ and the vacuum separation, a It turns out that for a typical metal workfunction of $4 \rightarrow 5\text{eV}$, the separation of the metals, a , must be of the order of Angstroms for tunnelling to occur

1.2 The Scanning Tunnelling Microscope

Scanning tunnelling microscopy reveals three dimensional pictures of surfaces right down to atomic scales The STM experiment [1] involves bringing a sharp metal tip, which is biased with respect to the sample, close enough to the sample surface that the gap between them is sufficiently small ($< 10\text{\AA}$) so electrons can quantum mechanically tunnel through the gap, as discussed in the previous section The exponential dependence of the tunnel current on distance (see eqn 1 1) means that the current is extremely sensitive to the tunnel gap, i.e. a small variation in tip-sample distance will correspond to a relatively large variation in the tunnel current This enables the high resolution attainable using the STM

The position of the STM tip is accurately controlled in three dimensions by piezoelectric drivers The tip is scanned in the two lateral dimensions, (x,y) , while the current between the tip and surface is monitored by the STM electronics A feedback network within the electronics changes the height of the tip, z , by applying biases to the piezoelectric controllers, to keep the current constant An STM image is therefore built up by plotting each value of z to its corresponding lateral position in (x,y) This mode of operation is commonly referred to as '*constant current*' mode The other commonly used mode of operation is '*constant height*' mode The difference with this mode of operation is that the tip is kept at a constant height above the sample surface and the variation in

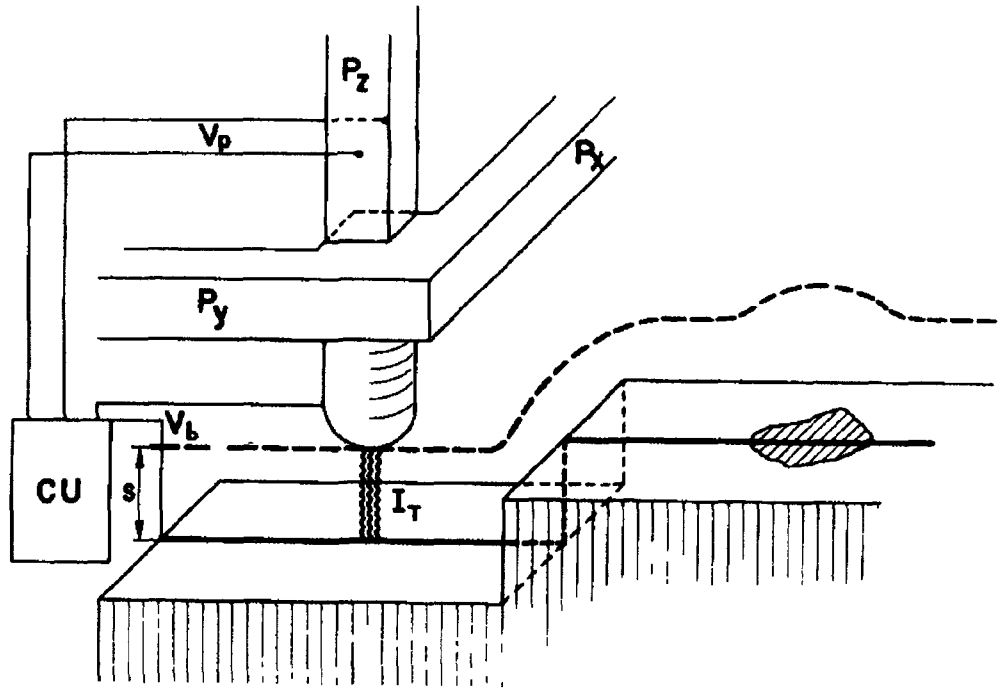


Fig 1 3 Schematic of the STM experiment (afterRef [1])

tunnel current as the tip is rastered across the surface is monitored. The advantage with the *constant height* mode of operation is that the tip can be scanned at a faster rate which may be of use when studying unstable surfaces. The faster scan rate is possible because in *constant current* mode there is a slight time delay as the feedback electronics adjust the tip height in order that the tunnel current remains constant. However the disadvantage with the *constant height* mode of operation is that a very flat surface is required (a peak to valley roughness of $<5\text{-}6\text{\AA}$) otherwise the tip is liable to come in contact with the surface (tip crash) which very often damages the tip considerably resulting in loss of resolution or very poor quality images.

The resolution of the STM is determined by the tip, because the tip is of finite radius the surface topography can only be determined with a finite resolution. A simple estimation of the resolution can be made as suggested by Tersoff et al [2]. Assuming a parabolic tip of radius R , and tip-sample separation d , a point on the surface x , will

correspond to a point on the tip of height $d+x^2/2R$. The corresponding current at that point from eqn (1.1) will be $I \propto \exp(-\kappa x^2/R)$. Tersoff [2] has shown that the instrument resolution, δ , can be given by the equation,

$$\delta = [2\kappa^{-1}(R+d)]^{1/2} \quad (1.3)$$

Since κ is typically 1 \AA^{-1} , even a large tip radius of say 1000 \AA would give a resolution of $< 50 \text{ \AA}$.

1.3 Scanning Tunnelling Spectroscopy

The theory of tunnelling in one dimension for planar bulk tunnel junctions was developed in section 1.1 and this will serve as our starting point for understanding tunnelling spectroscopy from a theoretical stand point.

1.3.1 Current-Voltage(I-V) spectroscopy.

It can be seen from Fig 1.2 that applying a bias voltage, V , to the sample can cause the energy levels of the sample to shift relative to the energy levels of the tip by an amount qV (where q is the charge of an electron). The polarity of the applied bias determines whether the sample energy levels shift up or down. If we first take the case of a metal tip imaging a metal surface. At positive sample bias the net tunnel current arises from electrons tunnelling from the occupied states of the tip to the unoccupied states of the sample, as in Fig 1.2(b). At negative sample biases the reverse is the case with tunnelling from occupied states of the sample to the unoccupied states of the tip.

The I-V spectroscopic technique involves placing the tip over a certain region of the surface, ramping the voltage from positive to negative bias and monitoring the current at various voltages. For the situation considered above we would expect to see the current increase exponentially with increasing bias as in Fig 1.4. The reason for the exponential increase comes from equations 1.1 and 1.2, as it can be seen that the transmission of electrons across the barrier has an exponential dependence on κ . As κ is dependent on the barrier height ($V_0 - [E + qV]$), an increase in the applied bias, V will cause an exponential increase in the transmission probability.

If we now consider the case for I-V spectroscopy of an intrinsic semiconductor surface. We use the metal-insulator-semiconductor approximation and ignore any band bending at

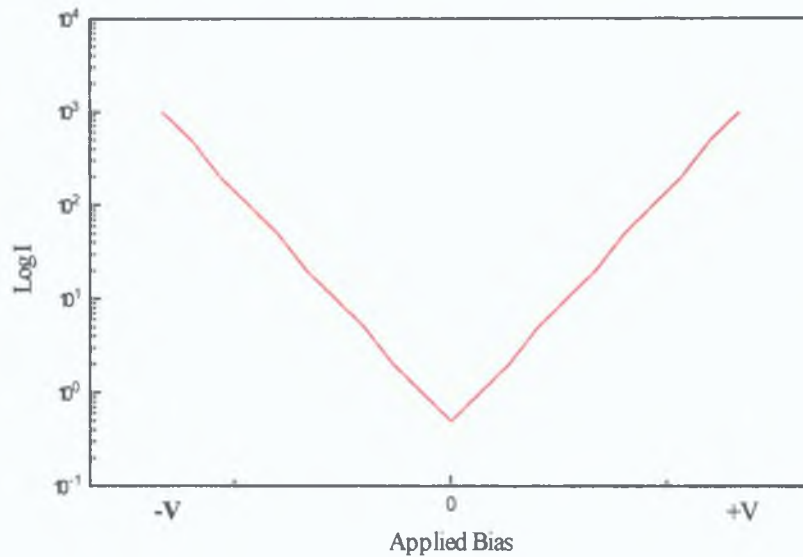


Fig 1.4 Expected I-V plot for metal-vacuum-metal system.

the semiconductor surface from either tip-induced band bending or pinning of the surface Fermi level due to surface energy states. Fig 1.5(a) shows the energy level diagrams for such a system in thermodynamic equilibrium. Applying a small negative bias ($-qV < E_g/2$, where E_g is the semiconductor bandgap) one would not expect any significant increase in tunnel current because there are no occupied states in the bandgap of the semiconductor for electrons to tunnel from, into the metal (as in Fig 1.5(b)). However increasing the applied negative bias such that, $-qV > E_g/2$ a large increase in current would be expected as electrons tunnel from the semiconductor valence band into the unoccupied states above the tip Fermi level (see Fig 1.5(c)). Reversing the polarity of the applied bias such that the sample is positively biased, again we would not expect to see any significant increase in the measured current until $qV > E_g/2$, at which point the current would increase exponentially with increasing applied bias. Fig 1.6(a) shows the expected I-V plot for an intrinsic semiconductor.

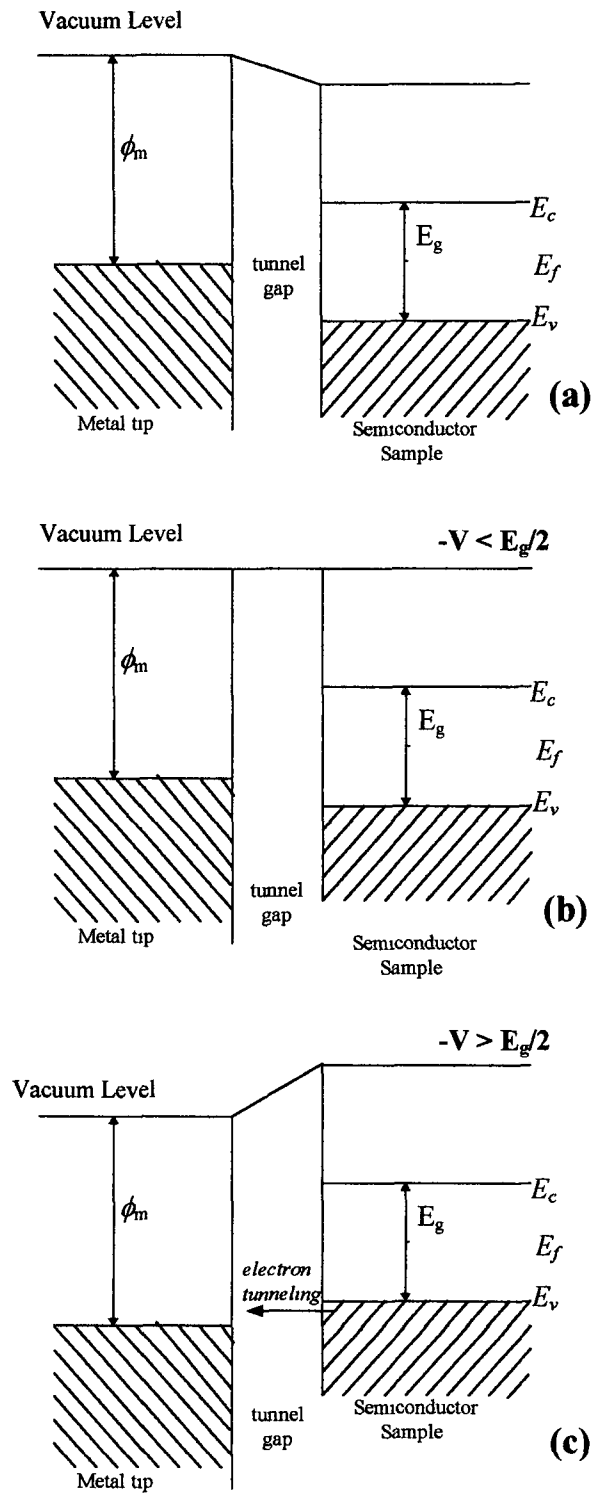


Fig 1.5 Energy level diagrams for a metal-insulator-semiconductor system at (a) thermodynamic equilibrium, (b) low negative bias and (c) high negative bias

For an extrinsic semiconductor the only difference in the I-V plot from that of the intrinsic semiconductor would be the contribution to the tunnel current from the dopant induced states. This contribution for a moderately doped n-type semiconductor

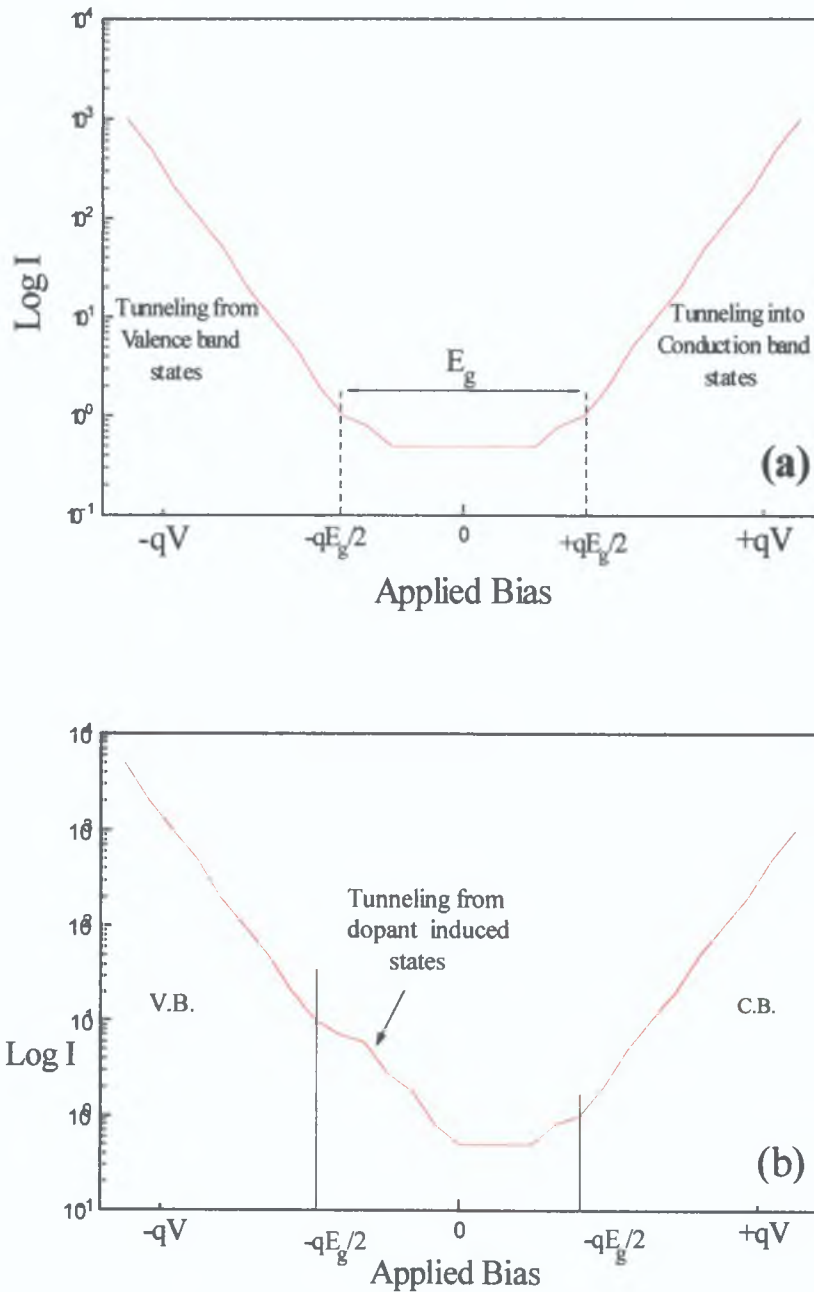


Fig 1.6 Expected I-V plots for (a) intrinsic, (b) extrinsic semiconductor.

would be a result of tunnelling from the dopant states into the unoccupied tip states for low negative biases, where $qV < E_g/2$. The effect on the expected I-V curve can be seen in Fig 1.6(b), where there is an increase in the measured current between $-E_g/2 < qV < 0$.

1.3.2 Current-Distance(I-S) spectroscopy.

In the WKB tunnelling formula for planar electrodes the tunnelling transmission probability, $T(E, eV)$, for electrons with energy, E and applied bias voltage, V is given by the expression [3]

$$T(E, eV, r) = \exp\left(-\frac{2Z\sqrt{2m}}{\hbar} \sqrt{\frac{\phi_s + \phi_t}{2} + \frac{eV}{2} - E}\right) \dots(1.4)$$

where ϕ_s and ϕ_t are the local workfunction of tip and sample respectively,

Z is the tip-sample separation,

m = mass of an electron, $\hbar = h/2\pi$ and h is Planck's constant.

At low bias voltages, eV is approximately zero and $E = E_F$ so equation 1.4 simplifies to

$$T = \exp\left(\frac{2Z\sqrt{2m}}{\hbar} \sqrt{\frac{\phi_s + \phi_t}{2}}\right) \dots (1.5)$$

Thus the tunnelling transmission probability can be directly related to the local workfunction of the sample, ϕ_s . In the planar tunnelling model the current is given by [3]

$$I = \int_0^{eV} \rho_s(r, E) \rho_t(r, -eV + E) T(E, eV, r) dE \dots (1.6)$$

where ρ_s and ρ_t are the density of states of tip and sample respectively, at location r , and with energy, E measured with respect to the Fermi level.

From equations 1.4 and 1.5 it can be shown that

$$\frac{dI}{dZ} = \frac{2\sqrt{2m}}{\hbar} \sqrt{\bar{\phi}} \dots(1.7)$$

where $\bar{\phi}$ is the average workfunction of the tip and sample.

Thus displacing the tip vertically in the z -direction and monitoring the variation in current at a fixed bias the average work function of tip and sample can be determined.

From Fig 1.2 it can be seen that the average workfunction is a good approximation of the effective tunnel barrier. Thus, one can obtain an approximate value for the effective or apparent barrier height by rearranging eqn 1.7 to its more commonly used format

$$\phi_b (eV) = 0.952 \left(\frac{d \ln I}{dz} \right)^2 \quad (1.8)$$

where $\phi_b \cong \bar{\phi}$

Assuming the workfunction of the tip to be constant, variations in ϕ_b at different points at the surface can be attributed to changes in the local workfunction.

References.

- 1 R Binnig, H Rohrer, C H Gerber, E Weibel, Phys Rev Lett 49 (1982) 57
- 2 J Tersoff, D R Hamann, Phys Rev Lett 50 (25) (1983) 1998
- 3 D Bonnell, Scanning tunnelling Microscopy and Spectroscopy, (VCH Publishers, Cambridge, 1993), Pg 95

Chapter 2 : Experimental systems and techniques

2.1 The Nanoscope II air STM.

2.1.1 Instrumentation

The Nanoscope II air STM is a commercially available STM produced by Digital Instruments, California. It consists of three major components - the actual microscope head and base unit (shown in Fig 2.1), the control unit and the computer workstation. These components are illustrated schematically in Fig 2.2. The STM 'head' consists of a piezoelectric tube scanner encased in a stainless steel surround with a mounted pre-amplifier. Coarse adjust screws enable the tip position above the sample head to be adjusted, with a stepper motor controlling a fine approach screw at the back of the head.

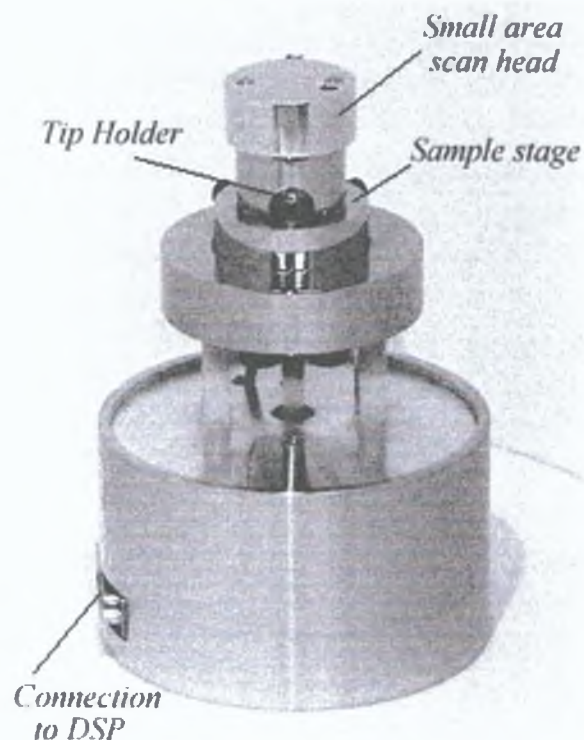


Fig 2.1 Picture of Nanoscope II air STM scanner.

Both the raster scan and the feedback control loop are controlled by a Digital Signal Processor (DSP) in the workstation. This DSP passes height and/or current data to the 80386 Central Processing Unit (CPU) and graphics processor in the workstation for display or storage. The feedback loop passes from the microscope through the control unit to the DSP and back again.

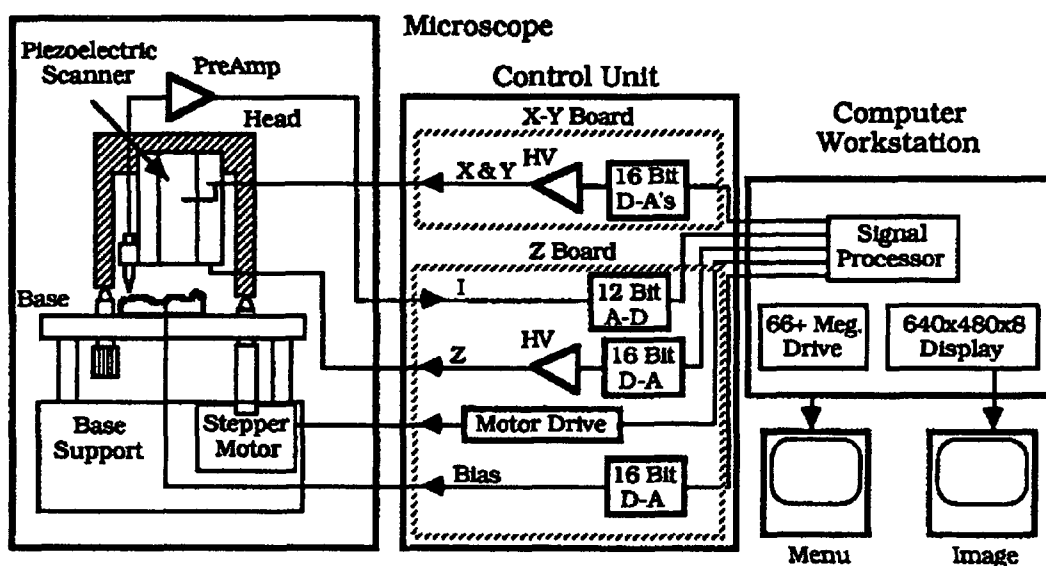


Fig 2 2 Schematic diagram of the Nanoscope II air STM

The tunnelling current from the microscope enters the control unit and is sampled at a rate of 63 kHz, converted to a digital binary representation and transmitted over a flat ribbon cable to the DSP. The DSP then uses this value to calculate a new height value which is transmitted back to the control unit. It is then converted to an analogue signal, amplified with a high voltage amplifier and applied to the z electrode of the piezoelectric scanner. Mounted on the front of the head is a 0.012 inch bore stainless steel tube which is inside the ceramic tip holder as seen in Fig 2.1. The tip holder is designed for tips that are 0.010 of an inch in diameter. The tips used were all either W or PtIr 0.010" 'Nanotips' also supplied by Digital Instruments. Before inserting the tips into the tip holder they had to be 'kinked' in order to ensure the tips were securely positioned.

2.1.2 Image Acquisition.

The Nanoscope STM takes images by scanning the tip across the surface in a raster fashion. The tip is first scanned in the X direction from right to left and the corresponding tip height (or tunnel current) at that position is shown on the screen. At the end of the X scan the tip is displaced in the Y direction and on the screen the Y position is incremented and the tip is again scanned in X across the sample.

In constant height mode while the tip is scanning the tunnel current is sampled. Any deviation in the tunnel current from the setpoint is run through a proportional-integral feedback calculation and the tip height is adjusted to maintain tunneling at the setpoint current.

The Nanoscope II software supports three different sampling densities, 400x400, 200x200 and 100x100. The accumulated images therefore will have differing pixel resolution depending on the sampling density chosen. The 400x400 point images will offer the highest pixel resolution. This can be understood by considering a 2 x 2 μm image for which the corresponding interpixel distance will be 5nm for a 400x400 point image, while for a 100x100 point image of the same area the interpixel distance will be 20nm. The disadvantage with using the 400x400 point images is that they have only half the frame rate of the 200x200 point image at a given scan rate. This means the 400x400 point images are more suitable for stable surfaces.

2.1.3 Calibration considerations

Correlation of the imaged area and heights to the true values of the area and heights scanned, is dependant upon the setting of the X, Y and Z sensitivities. The Nanoscope software enables the user to adjust these settings (given in Angstroms/volt) should there be a problem with measurements made from STM images.

Another parameter crucial to the measurements made using STM images is the derating. This parameter mainly affects large area scan heads, because as the scan areas increase the non-linearity of the piezos can become a problem. For example, for a large area scan head a plot of the head sensitivity as a function of scan area would indicate that the head loses sensitivity as the scan voltage is reduced. To compensate for this effect the Nanoscope software has X and Y derating settings which are used

to calculate the true scan area as the scan size is reduced. The derating value is taken as the slope of a plot of the head sensitivity versus scan area.

2.1.4 Acquisition of Spectroscopic data.

Making an I-V spectroscopic measurement involves first setting sample voltage and the feedback loop is then run to establish the setpoint current. Once this has been established the feedback loop is turned off and the tip maintained at this position and height for the remaining duration of the I-V scan. The bias voltage is then ramped within pre-set limits and the corresponding currents measured. The Nanoscope software allows the user take a number of consecutive scans and averages them before displaying as one data set. All the scans taken for this thesis used the average of 10 scans per I-V plot, and generally 5 of these I-V curves were taken consecutively to ensure repeatability.

Taking an I-S spectroscopic plot involves again setting sample voltage and the feedback loop is then run to establish the setpoint current. At this point the feedback loop is turned off and the bias voltage is held constant. The tip is moved away from the surface and then back the same distance again sampling the tunnel current (at 200 points) as a function of separation. For this thesis, the average of 10 scans per I-S plot, and generally 3 of these I-S curves were taken and averaged before using them for apparent barrier height calculations.

2.2 X-ray Photoemission Spectroscopy.

The X-ray Photoemission Spectroscopy (XPS) system is a Clam 100 spectrometer with a Model 849 analyser, which is a 100mm mean radius of curvature 150° spherical sector analyser fitted with a single channel electron multiplier detector and four pairs of externally adjustable slits of 4, 2, 1 and 0.5 mm (inlet and exit equal). Most work can be done with the 4mm slits and control of resolution can be achieved by varying the pass energy of the analyser. The system at Dublin City University the CLAM100 from VG Scientific is shown in Fig 2.3.

For all of the XPS spectra presented in this thesis the $K\alpha$ doublet of Aluminium, which has an energy of 1486.6 eV and a composite linewidth of ~ 0.85 eV FWHM, was used. Al x-ray sources are usually operated at an anode voltage of 15 kV and a current of 20 mA, to produce sufficiently intense photoelectron peaks.

CLAM 100 – COMBINED LENS ANALYSER MODULE

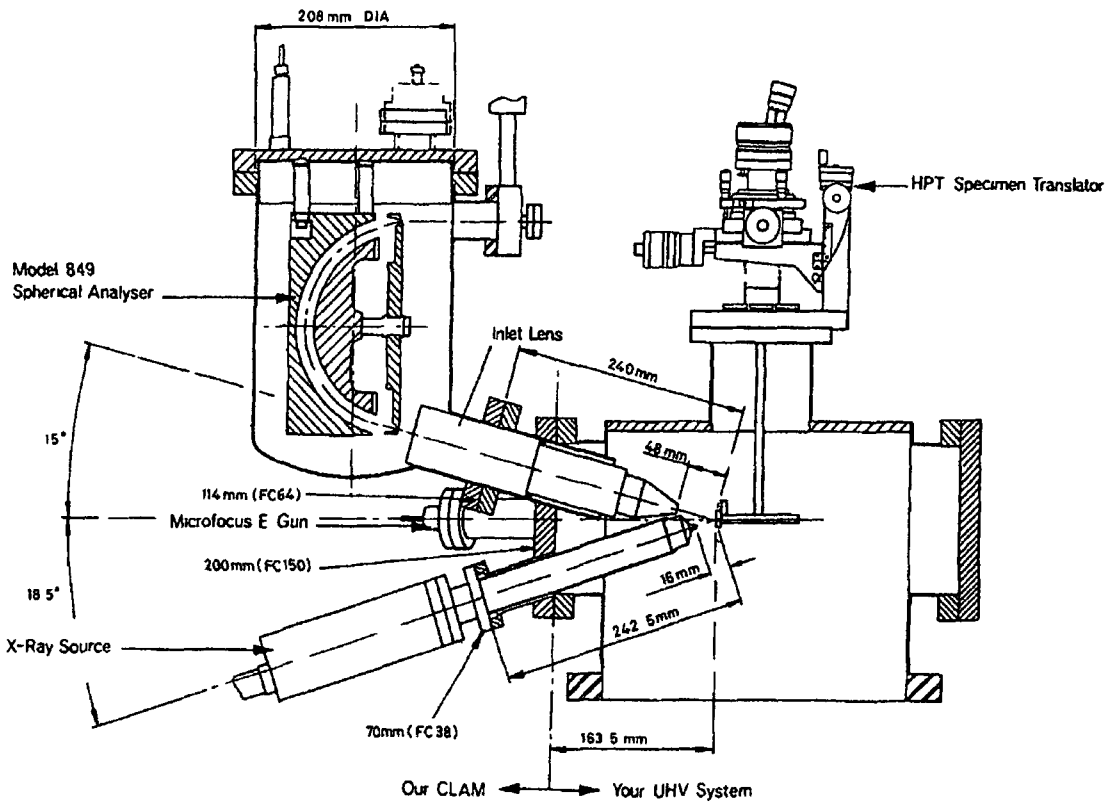


Fig 2.3 Schematic of Clam 100 from VG Scientific

The detector used, as mentioned above was a single channel electron multiplier or channeltron. The final output from the multiplier is a series of pulses that are fed into a dedicated electronic control unit, where it is usually D-to-A converted and displayed on a computer screen. The system uses the commercially available VGX900 software acquisition and processing package.

Chapter 3 : Calibration of the STM .

3.1 Introduction .

As semiconductor device technology advances and the critical dimensions decrease conventional metrological techniques, such as stylus profileometers, fall short in their ability to meet the required resolving power. The scanning tunnelling microscope (STM) is an instrument that has the potential to provide three-dimensional measurements with superior resolution to the aforementioned technique. The STM has the added advantages of being a non-destructive technique and samples require no pre-treatment, the only requirement being that the material is at least a moderate conductor.

This study investigates the metrological applications of a STM scan head which has a maximum scan area of $(100\mu\text{m})^2$. The measurements were made on calibration standards which have been designed as a STM calibration artefact and is certified by the US National Institute of Standards and Technology (NIST). In the first part of the study the effect of the STM tip profile on the measurements being made is investigated. The second part compares measurements made using two different methods of measurement analysis and assess the resolution and accuracy achievable with this STM.

3.2 Influence of the tip on the measurement process

The STM tip has been shown to affect the resolution of the STM [1] and also contribute to the resulting image [2]. In section 1.2 a method for calculating a value for the resolution of the tip, δ was presented ($\delta = [2\kappa^{-1}(R + s)]^{1/2}$ equation 1.3) following the method of Tersoff et al [3]. However, this equation requires the knowledge of the tip radius R , the tip-sample separation s , and κ (where $\kappa^2 = \frac{2m}{\hbar^2}(\bar{\phi} - E)$ as in equation 1.2). At low tip sample separations, $s \leq 5\text{\AA}$ and a tip radius $R \geq 2\text{nm}$, R and κ become the most significant parameters in the calculation of the instrument resolution from equation 1.3. A value for κ can be established from I-S spectroscopy, since the tunnel current $I \propto \exp^{-\kappa s}$ by simply fitting the I-S curve with an exponential decay, a value for κ can be extracted. A method of estimating an upper limit for the tip shape was proposed by Reiss et al [1].

Vancea et al [4] had previously shown that Au coated cleaved single crystalline NaCl shows large cleavage steps. These steps are large and steep single steps up to about 80nm in height. Imaging the sharp edge of such a step on this surface it became evident that the image did not show this cornered form, but will give an upside down picture of half of the tip. This effect can be seen in Fig 3 1 where between points 1 and 2 the image will be distorted due to the tip shape.

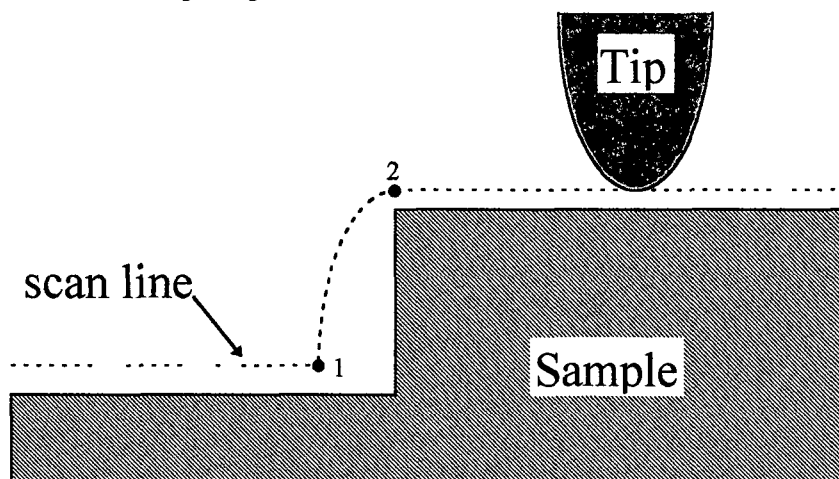


Fig 3 1 Scan line produced by a blunt probe encountering a sudden step (after Ref [5])

Even if the upper edge of the cleavage step is not atomically sharp, the effect on the image of the tip is that it will be slightly smeared out. Either way this method of evaluating the tip shape can provide a reliable upper estimate of the effective shape of the tip. Fig 3 2 shows a 3-D surface plot of the Au coated NaCl surface imaged with a PtIr tip, showing a 20nm cleavage step.

Fig 3 3 shows the estimated tip shape obtained from the cleavage step shown in Fig 3 2. The tip shape shown in Fig 3 3 was generated by firstly taking profiles normal to the step, inverting the profiles and then mirroring the profile of the step about the point where the step starts. To obtain an upper limit of the tip effective radius a procedure was developed which involved the fitting of the data using two parabolic curves. The first method [6] is that the tip radius, R , is obtained from the equation,

$$tip(x) = x^2/R \quad (3.1)$$



Fig 3.2. (160nm)² STM image of a cleavage step on an Au coated NaCl crystal, with the vertical range shown on the left in nm.

For this curve fit we obtain a value of 4.8 nm for the tip radius. The second method is that used by Reiss et al [1] where,

$$tip(x) = \alpha x^2 / (1 + \beta |x|) \dots (3.2)$$

where $R = 1/2\alpha$ and the cone angle, $\varphi = \arctan(\alpha/\beta)$.

Using this equation the value of the tip radius, R was estimated to be 3.5 nm and the cone angle of the tip 45°.

I-S spectroscopic plots of the Pt coated surface surrounding the calibration grids yielded a value of $\kappa = 0.34 \text{ \AA}^{-1}$. The tip was deemed to have crashed at a tunnelling current of $\approx 2.9 \text{ nA}$, thus an approximate value for the tip-sample separation, s for $I_t = 1 \text{ nA}$ would be, $s \approx 3 \text{ \AA}$. From these estimated values and equation 1.3 the upper limit on the resolution (δ) achievable with the STM using a PtIr tip was calculated to be, $\delta \approx 0.5 \text{ nm}$.

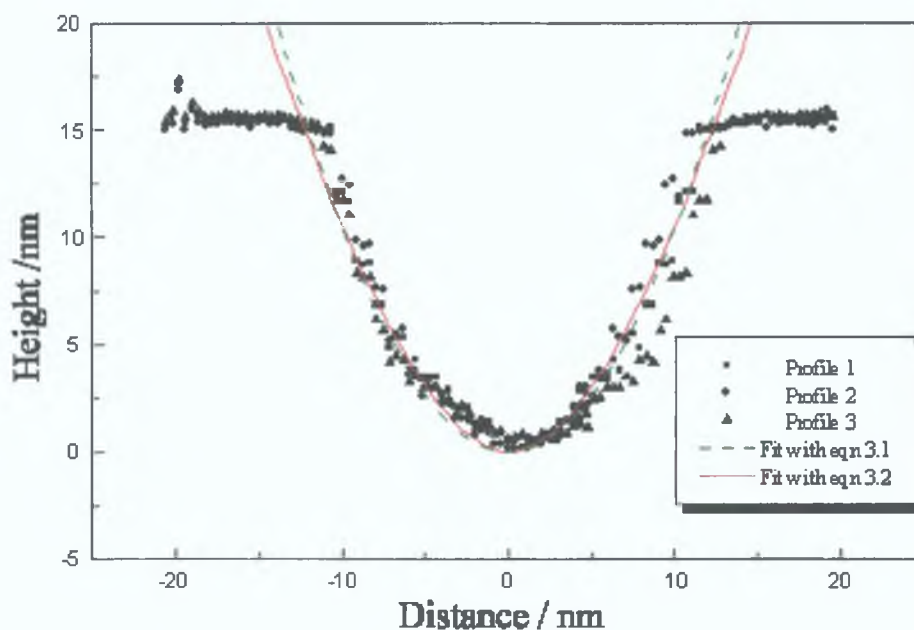


Fig 3.3. Estimated tip shape from cleavage steps of the Au coated single crystalline NaCl. Included are parabolic curve fits of tip shape.

This value of δ , however, holds only assuming the surface roughness is of the order of nanometers. Fig 3.4(a) shows profiles taken from scans of the 3, 10 and 20 μm pitch grids. In Fig 3.4(b) we see the actual shape of the step from the grid manufacturers specifications. From these plots it is clear that while the 10 and 20 μm pitch grids are well resolved, the 3 μm pitch grid is poorly defined. This limitation we believe is due to the STM tip.

To illustrate this point more clearly in Fig 3.5(b) we simulated the ideal profile of the 3 μm pitch grid and compared to a profile of that grid obtained using the STM.

The simulated profile was calculated by first obtaining a value for the slope of the step face. This was done by least squares fitting the left hand side of several steps from scans of the 3 μm pitch grid. A value of 0.129 ± 0.002 was calculated for the slope. The height of each step is known to be 100 nm, so from this for each pitch there are two slopes corresponding to a lateral distance of 775 nm as shown in Fig 3.5(a). From this the top and base sections of the profile wells were calculated to be a distance of 725 nm.

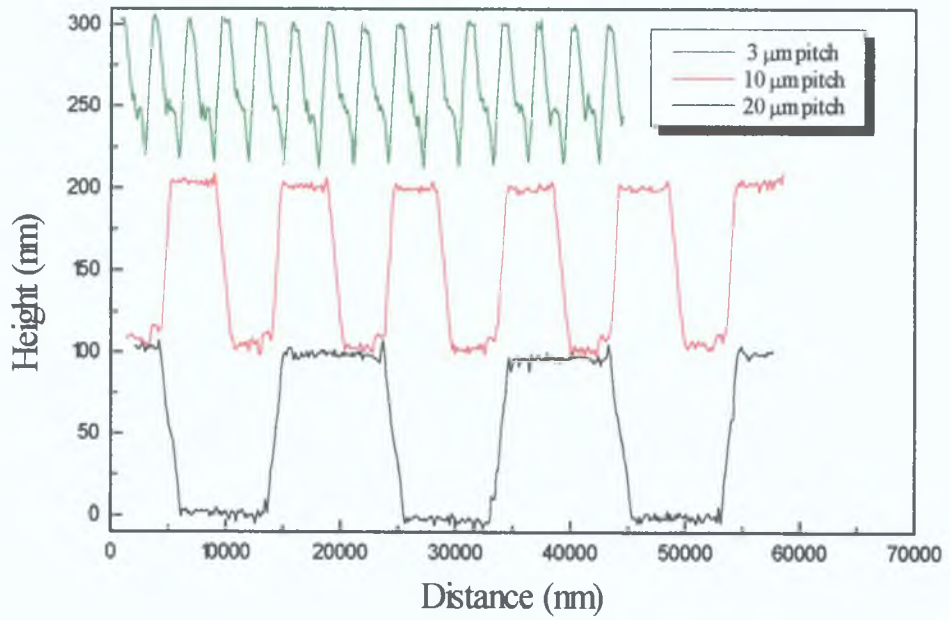


Fig 3.4(a). Sample profiles taken from STM images of 3, 10 and 20 μ m pitch calibration grids

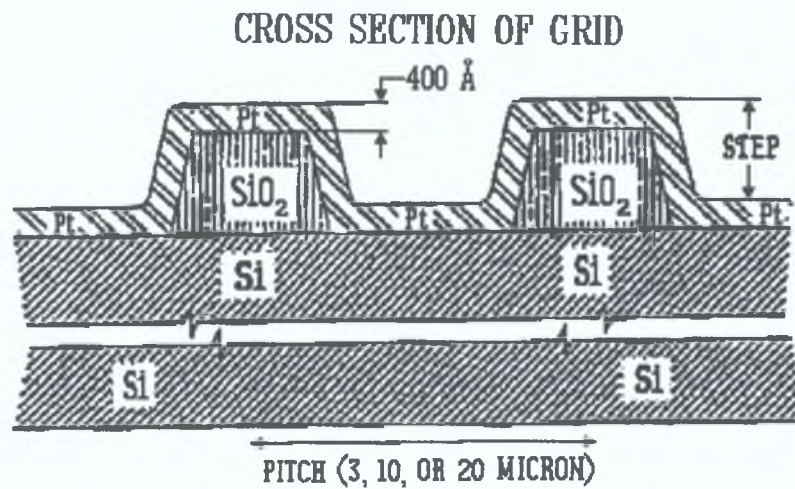


Fig 3.4(b). Actual shape of step from manufacturers specifications.

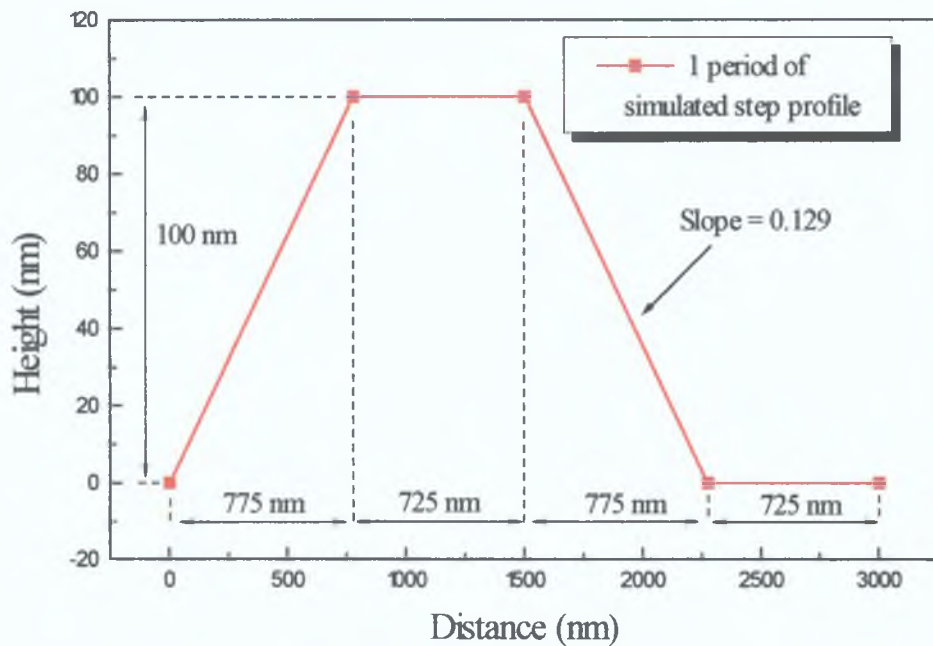


Fig 3.5(a) Simulated step profile of 3 μm pitch grid

From the profile taken from the STM image in Fig 3.5(b) we see that the profile does not reflect the true shape of the step above the dashed line, which is at about 40 nm above the base of the steps. The apparent difficulty in imaging the base of the step indicates that at 60nm from the tip apex, the tip width must be of the same order of magnitude as the base of the step.

In summation, the tip resolution can be thought to be < 1 nm, however, this appears to hold true for very flat surfaces or surfaces with features $> 1\mu\text{m}$, i.e. larger than the tip width, as became evident from the scans of the $3\mu\text{m}$ pitch grids. The effects of the tip on the measurement capabilities of the STM in the μm range will become clearer after repeatability studies of the measurement process have been carried out

3.3 Motivation for development of profile differentiation .

The method of taking measurements used for a previous calibration project [7] was to make Fast Fourier Transform measurements on the calibration artefacts. This method was employed because the STM, being a discrete sampling instrument, its real space

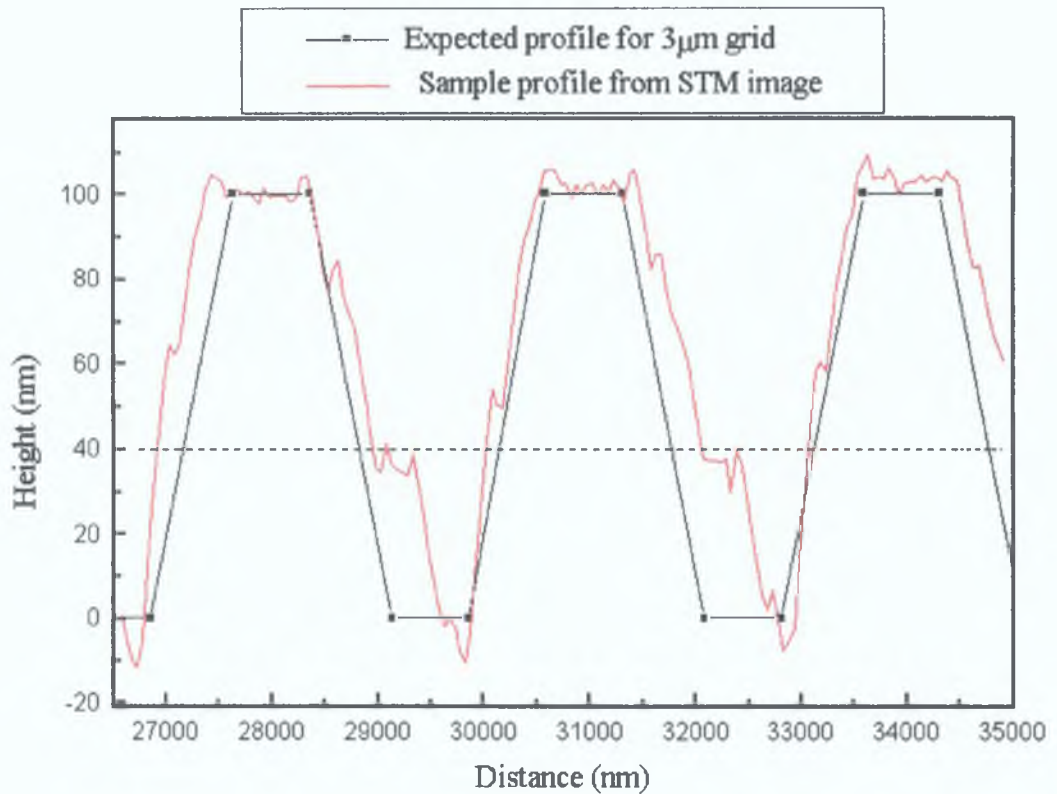


Fig 3.5(b). Comparison of simulated profile of 3 μm pitch grid and profile taken from 20 μm² scan of 3 μm pitch grid.

resolution (in Angstroms or nanometers) is determined fundamentally by number of points per scan and the scan area (or the interpixel distance of a stored scan, as mentioned in section 2.1.2). The advantage of this method was that it enabled measurements of the calibration artefacts' periodicity to be made at sub-pixel resolution. This is because the Fourier transform allows a transfer from a discrete measurement space (in this case distance) to a quasi-continuous domain (frequency or inverse space). However, using this technique metrological applications are limited to surfaces with a periodic nature. In order to avoid this limitation, the procedure developed in this study uses a software program to make automated measurements of STM images.

The method of taking measurements using the Nanoscope software is very subjective. Measurements taken require the user to,

- Select a profile using a mouse controlled cursor- which affects the measurements if the profile is not parallel to the grid edges.

- Use a mouse-controlled cursor to determine the length to be measured - which depends on both the mouse sensitivity and the interpixel distance of the image

Both of these steps are subjective procedures which will vary from user to user and are not very practical from a metrological point of view. Thus a more precise measurement technique would be to eliminate problems associated with this technique.

To eliminate the above problems a software program was developed that only allowed a profile used for pitch measurements to deviate by an angle of less than 0.5° from a reference line which was set parallel to the calibration grid edges. To eliminate the other problem introduced by the mouse the extracted profiles were first differentiated. From these differentiated profiles the pitch measurements were then made by measuring the distances between the peaks. The peaks on the differentiated profiles correspond to points where the slope of the profile flips, i.e. at a step. This helps eliminate systematic errors because there is only one choice for the values of the peak.

3.4 Surface Topography standards

The calibration grids used are manufactured by VLSI standards Inc. which are specifically designed as a calibration standard for Scanning Probe Microscopy and come with a calibration certificate. The standard consists of a silicon die with a pattern etched onto a $1\mu\text{m}$ silicon dioxide layer which is coated by 0.4 nm of Platinum for conductivity, see Fig 3.4(b). The pattern consists of three quadratic grids with $3\mu\text{m}$, $10\mu\text{m}$ and $20\mu\text{m}$ pitch lengths and a height of 100nm . Each grid pattern measures $270 \times 270\mu\text{m}$ and they are separated from each other by $100\mu\text{m}$. The VLSI standard was delivered with a certificate from the supplier and Table 2.1 shows the supplier's values, with the uncertainties shown in brackets.

Calibration Object	Suppliers Certificate	
	XY Pitch (μm)	Height (nm)
VLSI $3\mu\text{m}$ standard	2.99 (0.02)	98.5 (1.7)
VLSI $10\mu\text{m}$ standard	10.01 (0.02)	98.5 (1.7)
VLSI $20\mu\text{m}$ standard	20.00 (0.02)	98.5 (1.7)

Table 3.1

3.5 Program used to obtain measured values

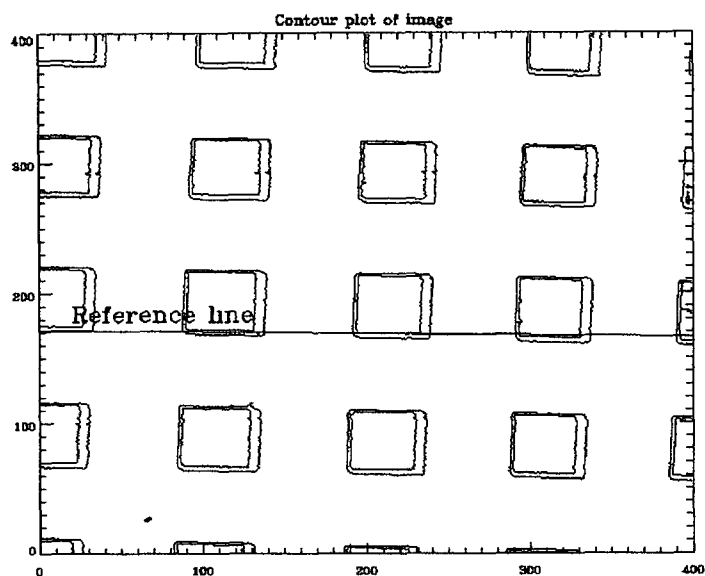
The program used for calculating pitch measurements via profile differentiation was written using IDL (Interactive Data Language) which ran on a UNIX operating system. The program first reads in an STM image and asks the user to set up a line parallel to the grid edges in the direction that the profile is to be taken. The reference line is drawn on a contour map and the user decides by visual inspection whether the line is suitable as a reference line or not (Fig 3 6). This line is then used as a reference line for all subsequent profiles taken. Should the user take a profile which has an angle that varies more than 0.5° from that of the reference line, the profile is disregarded and the user is prompted to take another profile. This was done because in an earlier study [7] which measured the periodicity of the grids using FFT's, it was discovered that a misorientation of 5° of the profile, lead to an increase in the error, for a $(30\mu\text{m})^2$ scan of the $3\mu\text{m}$ pitch grid, from $\pm 141\text{nm}$ to $\pm 197\text{nm}$.

Once a profile was accepted it was differentiated numerically using the formula

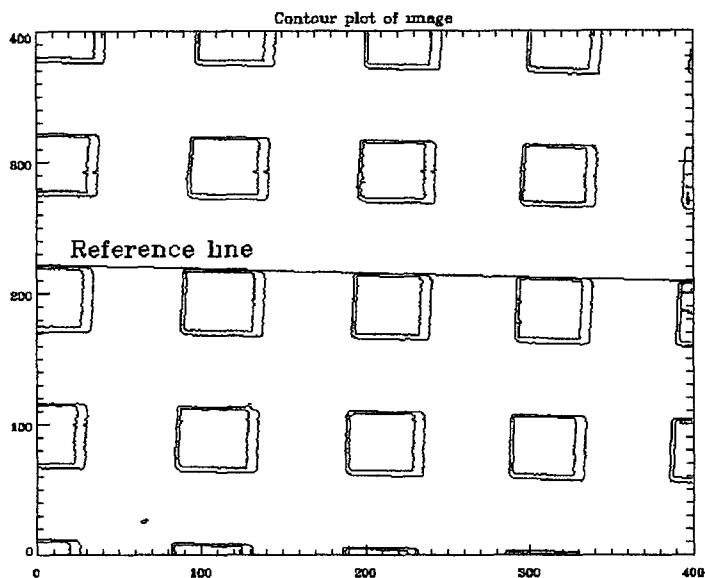
$$\frac{dy(i)}{dx} = \frac{[y(i+1) - y(i-1)]}{\Delta x} \quad (3.3)$$

The differentiated profile is then plotted on screen and the user is prompted to click on the each of peaks that they wish to use. The maximum in height of each peak is found and its corresponding value in x is stored. The pitch measurement is then the difference in x between consecutive peaks. Fig 3 7 shows a sample profile and its derivative.

The user is offered initially the choice of taking a single, 10 or 15 consecutive profiles. The option of 10 profiles is for repeatability measurements, in that 10 profiles are taken along the same grid line and the mean and standard deviation over the 10 measurements are calculated for each individual pitch measurement. The 15 profiles is for accuracy measurements. Profiles are taken from different parts of the stored scan and the mean and standard deviation of all the pitch measurements is obtained.



(a)



(b)

Fig 3 6 Contour plots of calibration grids with (a) unsuitable and (b) suitable reference lines

3.6 Experimental Conditions.

All scans were taken at room temperature in the constant height mode of the Nanoscope II using a large area scan head. The scan speeds used were low 1.02 → 0.6 Hz and the scans were left running for well over an hour to allow the piezoelectrics to stabilise. The bias voltage used was 100mV with a tunnel current of 1 nA.

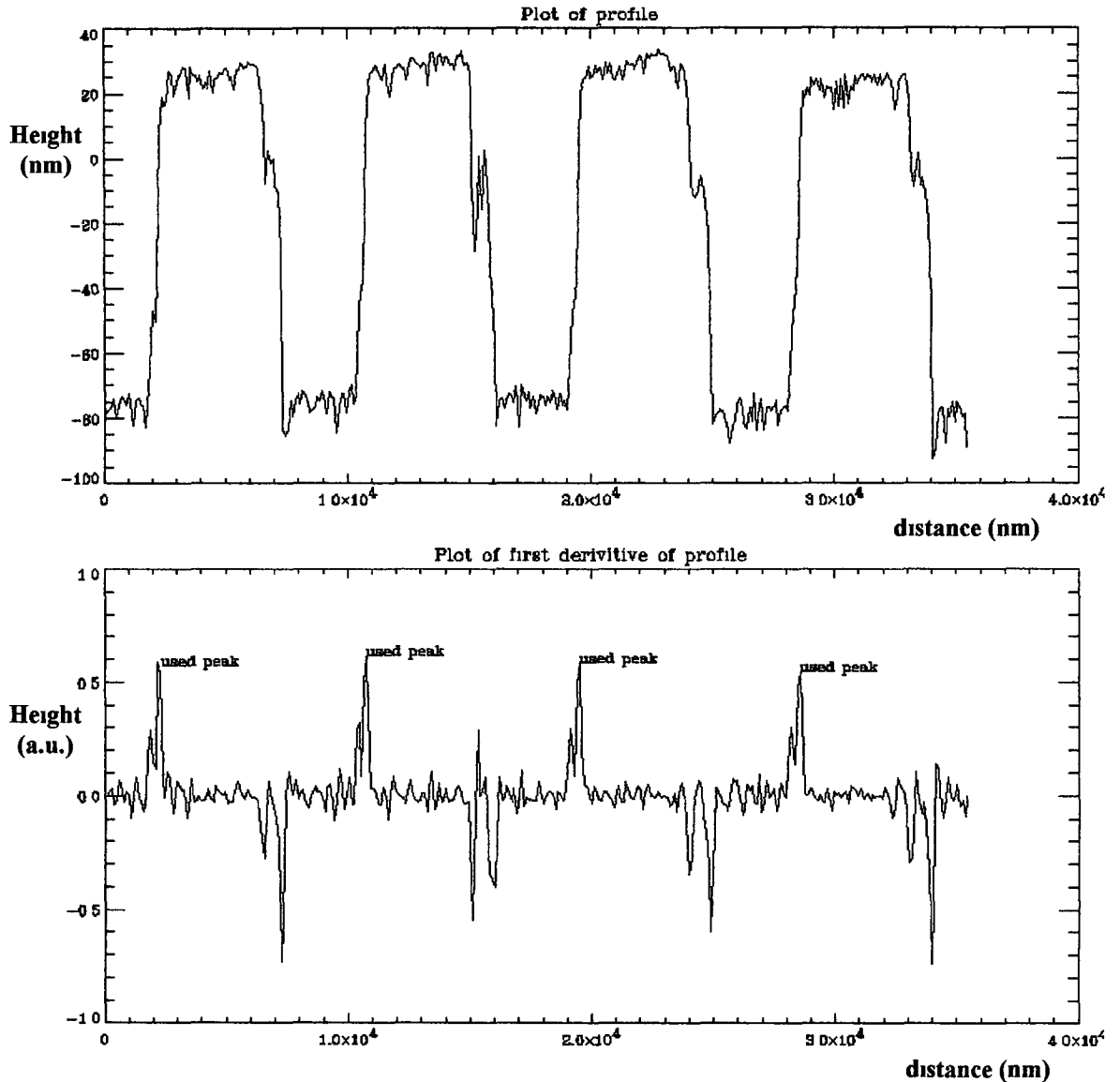


Fig 3 7 Sample profile from $(40\mu\text{m})^2$ scan of $10\mu\text{m}$ pitch grid(top) and its derivative(bottom)

3.7 Results

In this section three aspects relevant to the metrological capabilities of any instrument will be considered, the precision, accuracy and finally the degree of confidence in measurements taken. The precision of the instrument deals with the repeatability of measurements taken under given conditions, whereas the accuracy deals with how close the measured value is to the true value. Knowing the true value of our calibration

standard and its uncertainties a confidence level can be estimated for measurements taken under given conditions

3.7.1 Precision of measurements.

In order to establish the precision of measurements taken with any particular tip, scans of the calibration grids were taken with the tip motion in the Y-direction turned off. Ideally this should enable the scanning of the same line of the grids repeatedly in the x-direction. To ensure there was minimal thermal drift of the piezoelectric controller the system was let stabilise by letting the STM scan for over an hour before storing the image to be analysed. The Nanoscope software stores up to 400 repeat scans across the measured line of the grid. For these measurements the repeatability was compared at the two extremes in scan area, i.e. $(95\mu\text{m})^2$ scans of the $20\mu\text{m}$ pitch grid and $(20\mu\text{m})^2$ scans of the $3\mu\text{m}$ pitch grid. These measurements were performed using both the PtIr and W tips.

From the data for the $(95\mu\text{m})^2$ scan (Table 3.2) we see that the repeatability, as determined by the standard deviations, for the tungsten tip is less than half the interpixel distance. While the standard deviations for the PtIr tip are higher, they are still well below the value of the interpixel distance. Thus, when imaging at this scan area, it is clear that the interpixel distance will be a more significant factor in limiting the resolution, than either of the tips used. This shows the value of developing the profile differentiation method for data analysis as opposed to manually using the mouse driven cursor which is limited in precision to the interpixel distance.

profile	Interpixel distance (nm)	Profile Differentiation (Tungsten tip)			Profile Differentiation (Pt-Ir tip)		
		X(nm)	Std Dev(nm)	error %	X(nm)	Std Dev(nm)	error %
1	237.5	19007.64	76.03	0.38	20242.95	173.30	0.86
2	237.5	19569.24	121.65	0.61	19959.37	123.39	0.62
3	237.5	19577.16	122.96	0.62	20819.66	144.45	0.73
4	237.5	20138.62	83.25	0.42	--	--	

Table 3.2 $(95\mu\text{m})^2$ scan of $20\mu\text{m}$ pitch grid

Table 3.3 presents the results for the $(20\mu\text{m})^2$ scans of $3\mu\text{m}$ pitch grid. From the profiles for the tungsten tip it appears that the tip was too wide to image the bases of the grid wells, particularly when compared with those obtained using PtIr tips as in Fig 3.8. Thus the tungsten tips used will be a significant factor affecting the resolution achievable on features imaged that are of the order of $3\mu\text{m}$ or less. The data obtained scanning with

profile	Interpixel distance (nm)	Profile Differentiation (Tungsten tip)		error %	Profile Differentiation (Pt-Ir tip)		error %
		X(nm)	Std. Dev(nm)		X(nm)	Std. Dev(nm)	
1	50	2927.99	41.13	1.37	3108.22	0.12	0.004
2	50	3086.32	126.04	4.22	3158.35	0.12	0.004
3	50	3055.95	118.88	3.95	3108.22	0.12	0.004
4	50	3203.51	48.72	1.63	3007.95	0.11	0.004

Table 3.3 $(20\mu\text{m})^2$ scan of $3\mu\text{m}$ pitch grid

the PtIr tips clearly indicates that the tip resolution will be an insignificant factor with regards to the resolving capabilities, particularly when compared with the interpixel distance for the same scans.

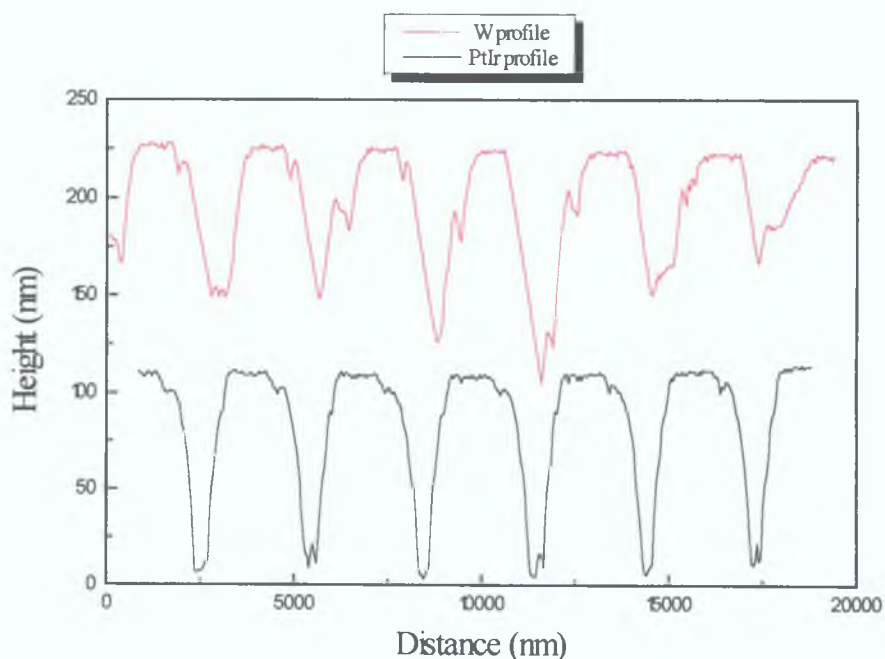


Fig 3.8 Comparison of profiles taken with W and PtIr tips taken from $(20\mu\text{m})^2$ scan of $3\mu\text{m}$ pitch grid.

In summary, it is clear that the standard deviation of the repeatability measurements is always less than the interpixel distance using the PtIr tip. However, the tungsten tip is unsuitable for measuring the 3 μ m pitch grid, which is illustrated by the poor quality of the tip profile as illustrated in Fig 3.8 and by the fact that in 50% of the measurements on this grid (see table 3.3) the standard deviation is greater than the interpixel distance.

3.7.2 Accuracy of Measurements.

The more important parameter to establish from the point of view of utilising the STM as a metrological instrument is the accuracy of any measurements made. To establish the accuracy of the profile differentiation method, 10 measurements were taken across three different grid lines of each scan in each direction. This meant, for example, at least 60 pitch measurements were made for a (60 μ m)² scan of a 20 μ m pitch grid. In using this procedure pitch measurements were taken from virtually all areas of the scans, which is important as unsuitable settings of the piezoelectric parameters may result in contraction or expansion of certain areas of the images and hence spurious measurements. The mean and standard deviation were then calculated for each set of measurements. These mean and standard deviation (shown in brackets) values are presented in Tables 3.4 to 3.9.

The tables also contain measurement data taken using the FFT method mentioned in section 3.3. For these measurements, FFT's were taken of three different profiles. The peaks of the three profiles were fit using a Gaussian curve. From the parameters of the fit curves the position of the peak was used to calculate the pitch measurement and the full width at half maximum was used to estimate the error in the measurements (as shown in brackets).

Scan size (μ m)	Interpixel distance (nm)	FFT method (Tungsten tip)		Profile Differentiation (Tungsten tip)	
		X(nm)	Y(nm)	X(nm)	Y(nm)
45x45	112.5	2943 (134)	2935 (136)	2947 (150)	2903 (70)
40x40	100	2952 (168)	2937 (172)	2980 (239)	2895 (99)
30x30	75	3031 (194)	2962 (185)	2975 (161)	2914 (159)
20x20	50	3021 (304)	3002 (289)	3014 (64)	2944 (36)

Table 3.4 Data for 3 μ m pitch grid imaged using tungsten tips

Scan size	Interpixel distance	FFT method (PtIr tip)		Profile Differentiation (PtIr tip)	
(μm)	(nm)	X(nm)	Y(nm)	X(nm)	Y(nm)
45x45	112.5	3030 (171)	3069 (165)	3046 (85)	3068 (63)
40x40	100	3070 (158)	3109 (167)	3029 (78)	3077 (67)
30x30	75	3068 (214)	3078 (216)	3052 (44)	3090 (54)
20x20	50	3095 (314)	3105 (324)	3084 (34)	3090 (47)

Table 3.5 Data for 3 μm pitch grid imaged using PtIr tips

Scan size	Interpixel distance	FFT method (Tungsten tip)		Profile Differentiation (Tungsten tip)	
(μm)	(nm)	X(nm)	Y(nm)	X(nm)	Y(nm)
80x80	200	9708 (875)	9523 (830)	9788 (179)	9695 (201)
60x60	150	9174 (1053)	9803 (1118)	9796 (161)	9682 (152)
40x40	100	9615 (1380)	8680 (1142)	9780 (189)	8779 (215)

Table 3.6 Data for 10 μm pitch grid imaged using tungsten tips

Scan size	Interpixel distance	FFT method (Pt-Ir tip)		Profile Differentiation (Pt-Ir tip)	
(μm)	(nm)	X(nm)	Y(nm)	X(nm)	Y(nm)
80x80	200	9487 (802)	9523 (718)	9846 (238)	9764 (180)
60x60	150	9920 (1172)	9661 (860)	9822 (210)	9718 (107)
40x40	100	9478 (1075)	9505 (951)	9883 (244)	9740 (94)

Table 3.7 Data for 10 μm pitch grid imaged using PtIr tips

Scan size	Interpixel distance	FFT method (Tungsten tip)		Profile Differentiation (Tungsten tip)	
(μm^2)	(nm)	X(nm)	Y(nm)	X(nm)	Y(nm)
95x95	237.5	19157 (2825)	18751 (2339)	19516 (397)	19395 (246)
80x80	200	19120 (3034)	19238 (2597)	19508 (309)	19309 (310)
60x60	150	19182 (3400)	19204 (4078)	19374 (222)	19401 (202)

Table 3.8 Data for 20 μm pitch grid imaged using tungsten tips

Scan size (μm)	Interpixel distance (nm)	FFT method (Pt-Ir tip)		Profile Differentiation (Pt-Ir tip)	
		X(nm)	Y(nm)	X(nm)	Y(nm)
95x95	237.5	20016 (3046)	20499 (4281)	20225 (328)	20482 (208)
80x80	200	19865 (2361)	19821 (2998)	20305 (420)	20476 (177)
60x60	150	19988 (3541)	19896 (3118)	19562 (1065)	19456 (168)

Table 3.9 Data for 20 μm pitch grid imaged using PtIr tips

From the tables some general comments can be made, the first being that the standard deviation of the measurements made using the profile differentiation method are always smaller than the error in the measurements made using the FFT method. Also the measurements made using the PtIr on the 3 μm pitch grid have lower standard deviations in both x and y directions than measurements made using the tungsten tip, while the opposite is the case for the 20 μm pitch grid. There seems to be little difference for measurements taken in the x and y-directions.

This data is analysed by first comparing the two methods used to make the measurements and secondly the overall accuracy achievable using the STM. In Fig 3.9 a comparison of the measurements made using the two different measurement techniques is presented, with the magnitude of the measurement error indicated by the error bars. Looking at the errors in the two measurements we see that for the FFT method the errors generally increase with decreasing scan size. This is understandable because at smaller scan sizes there are fewer pitch periods, this results in a broadening of the FFT peak and thus an increase in the error. The errors for the profile differentiation method generally decrease with decreasing scan size. This can be linked with the decrease in the interpixel distance as the scan area is reduced thereby leading to greater measurement accuracy. However, as the errors measured using the profile differentiation method do not always decrease with reducing scan area, as is the case for measurements from Table 3.7 taken in the x-direction. Hence it is clear that the quality of individual images also can have a bearing on the measurements along with their uncertainties.

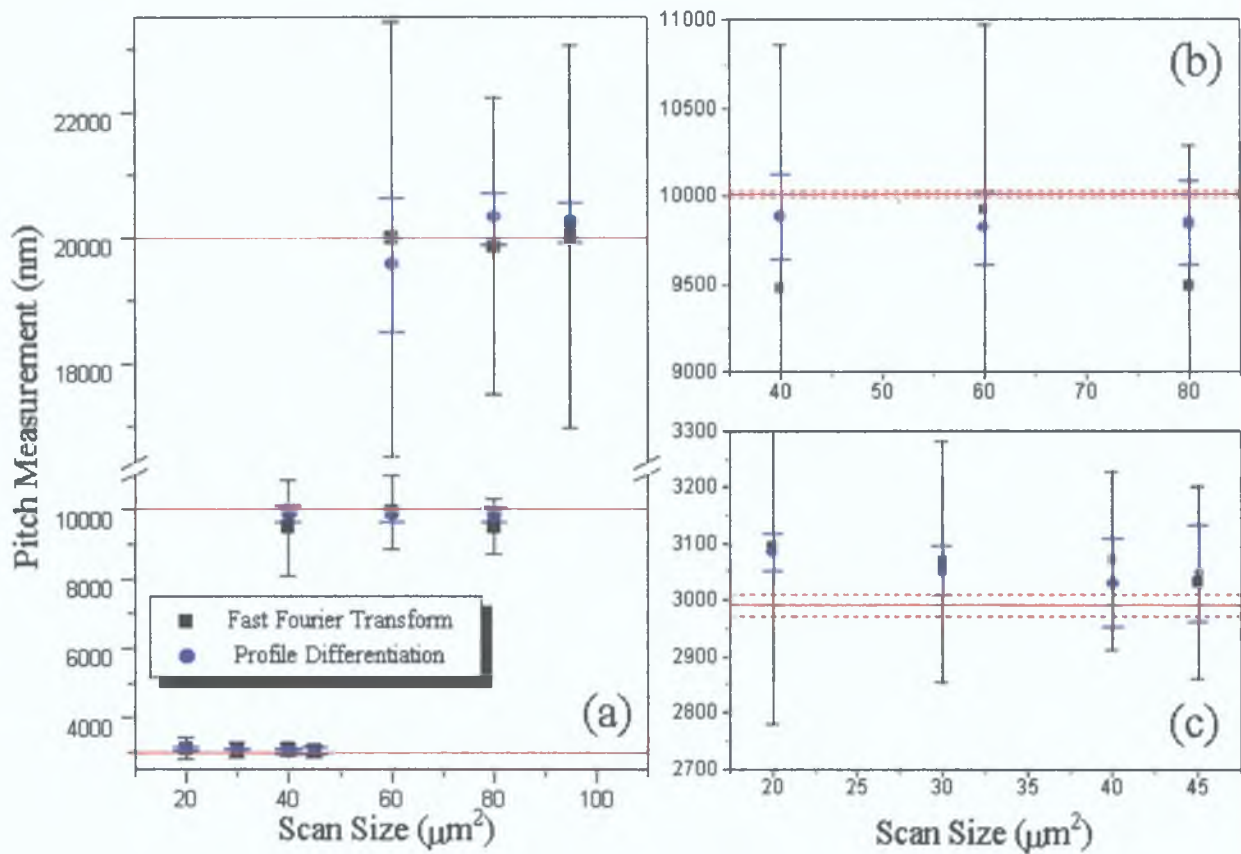


Fig 3.9 (a) Comparison of pitch measurements in the x-directions using a Pt-Ir tip taken via the profile differentiation and FFT methods for various scan areas. Included are specified pitch value (solid red lines) and tolerances (dashed red lines). (b) and (c) are expanded plots for the 10 μm and 3 μm pitch data respectively

The actual pitch measurements using the two techniques seem to have their closest correlation for the scans of the 3 μm pitch (Fig 3.9(c)) grid compared with those for the 20 and 10 μm pitch grids (Fig 3.9(a) and (b)). This could perhaps be explained again by the fact that fewer pitch periods broaden the FFT peak and lower the techniques resolving power. So as there would be 15 pitches for a (45 μm)² scan of the 3 μm grid compared with only 4 for a (95 μm)² scan of the 20 μm pitch grid, thus larger discrepancies between the two methods could be expected.

It is clear from looking at Tables 3.4 to 3.9 that as the pitch size increases from 3 to 20 μm that the FFT method results in significantly larger errors compared with measurements taken using the profile differentiation method. Errors of 20→25% are obtained for particular pitch measurements in Table 3.8 taken using the FFT method

while the profile differentiation method yielded errors of 1→3% for the same set of images

Comparing the accuracy of the two measurement techniques we see from Fig 3 9 that the majority of the measurements deviate significantly from the certified pitch values (solid red lines in fig 3 9) The large error in the measurements taken using the FFT method ensures that the true value lies within the bounds of the error However, as the error in the measurement is often greater than 10% of the actual value this is no great achievement The error in the measurements taken using the profile differentiation was typically less than 3% and from Fig 3 9 we see that only scans of the 3 μm pitch grid less than $(30 \mu\text{m})^2$ (which had errors < 1 5 %), were the values not within one standard deviation of the measured value

In Fig 3 10 we look more closely at the values obtained using the profile differentiation method The comparison is between values obtained using both tungsten and platinum iridium tips in both the x and y directions The error bars have not been included for clarity

From the measurements of the 20 μm pitch grid in Fig 3 10(a) we see that the measured values fall either side of the true value (solid red line) and similarly for the 3 μm pitch grid (Fig 3 10(c)), however, for the 10 μm pitch grid the values all fall short of the true value (Fig 3 10 (b)) This would appear to suggest that the derating function (see section 2 1 3) required to compensate for this would be non-linear, however, the Nanoscope II software would be unable to cope with such a requirement

It can also be seen from Fig 3 10 that the values measured in the x and y directions seem to correspond well But the values measured with the tungsten tips are almost always lower than the values measured with the PtIr tips We do not have any reasonable explanation as to why this is the case

3.7.3 Instrument Confidence.

In order to quantify the confidence level in any measurements made using the STM we must quantify the uncertainty in these measurements As the true values of the grid

itches (and its uncertainty limits) are known an error in the instrument measurements can also be expressed.

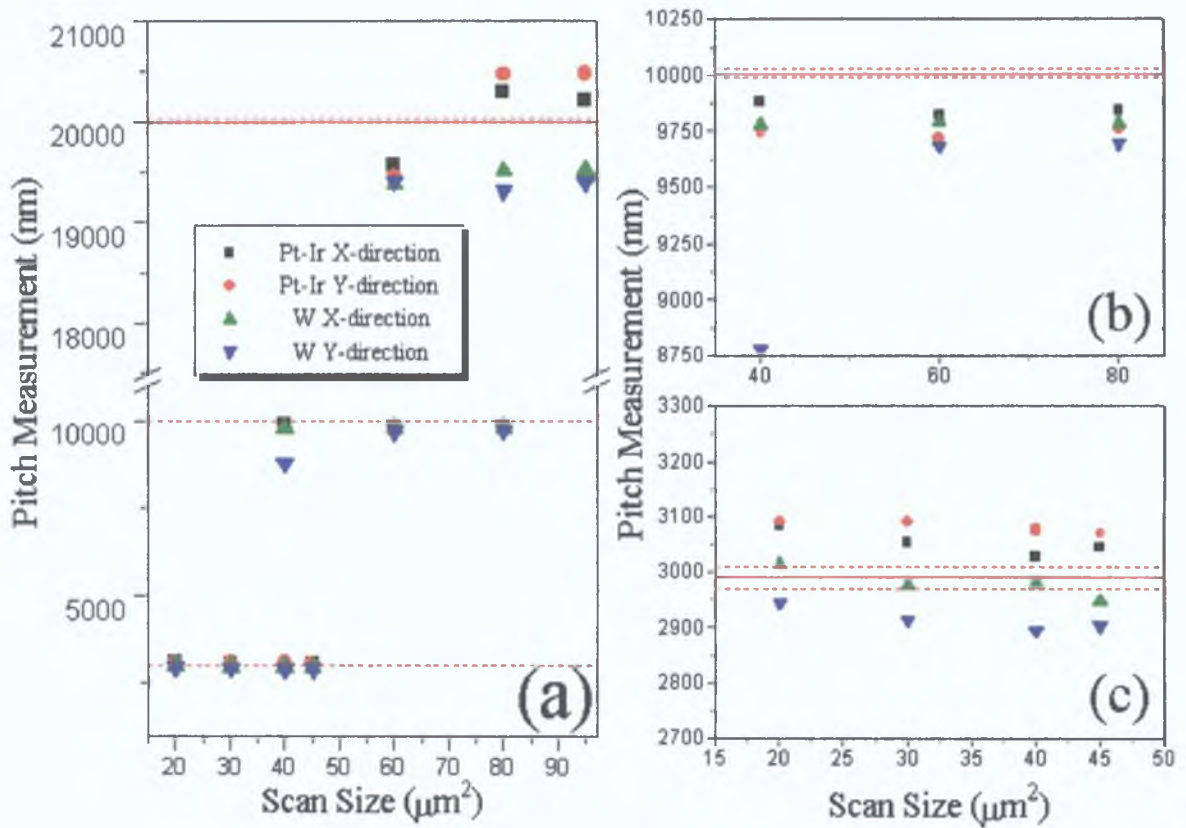


Fig 3.10 (a) Pitch measurements taken (profile differentiation) in x and y-directions from various scan areas using both Pt-Ir and W tips. Included are specified pitch value (solid red lines) and tolerances (dashed red lines). (b) and (c) are expanded plots for the 10 μm and 3 μm pitch data respectively.

The value of this instrument error is simply the difference between the true and measured value. However, in calculating the uncertainty we must define the confidence level required and the factors included in the uncertainty. Following reference [8], for > 45 repeated measurements (which covers all the measurements taken here) we can say that any measurement will lie within two standard deviations, s of the mean value, \bar{X} with a 95% confidence. Then for n measurements the mean, \bar{X} is defined as

$$\bar{X} = \frac{1}{n} \sum_{i=1}^n x_i, \dots (3.4)$$

where x_i is each measurement.

and the standard deviation s from the mean is,

$$s = \sqrt{\frac{1}{n-1} \sum_{i=1}^n (x_i - \bar{X})^2} \quad (3.5)$$

For a given standard deviation s as in equation 3.5 the standard uncertainty u for one measurement, x_i is given by the expression, [9]

$$u = \frac{s}{\sqrt{n}} \quad (3.6)$$

where n is the number of measurements made in determining the standard deviation, s . For a 95% confidence in the standard uncertainty, u , as with the standard deviation, for >45 measurements the standard uncertainty is simply multiplied by two.

The uncertainty in the pitch dimensions as quoted by the manufactures is 20 nm for all the pitch sizes. This is taken into account in our final estimate of the uncertainty by adding it to our standard uncertainty value, u which is calculated using equation 3.6. Table 3.10 shows the error and uncertainty at a 95% confidence level for scans of the 3 and 20 μm pitch grids taken using both tip types. The data was taken from tables 3.4, 3.5, 3.8 and 3.9 and the uncertainty calculated using equation 3.6.

Tip Type	Scan Area / μm	True pitch value (uncertainty) / nm	Pitch Measurement (Std. dev) / nm	error in measurement / nm	uncertainty at 95% confidence / nm
PtIr	30	2990 (20)	3052 (44)	62	33.3
Tungsten	20	2990 (20)	3014 (64)	24	36.5
PtIr	80	20000 (20)	20305 (420)	305	128.5
Tungsten	95	20000 (20)	19516 (397)	484	122.5

Table 3.10 Sample error and uncertainty values for STM measurements

These particular examples were taken to show the range of the instrument error and the uncertainty. Comparing the errors shown in table 3.10 there is an error in measurements made of approximately 2% (from ~60nm/3 μm and ~400nm/20 μm). Thus, for any measurement of a (30 μm)² area using a PtIr tip, the measurement would be given as

$$\text{measurement} - 62 \text{ nm} \pm 34 \text{ nm @ 95 \% confidence}$$

Note The uncertainty that would be introduced by the repeatability study (section 3.6.1) was omitted as only (95) and $(20\ \mu\text{m})^2$ scan areas had been undertaken in this section

3.8 Conclusions.

In this chapter the effects of our STM tips on the instruments resolution has been investigated and a calibration study of the STM was undertaken. It was shown that the tips are capable of resolving features of less than 1nm provided the features are only a few nm in height, as problems were encountered in resolving 100 nm steps of a 3 μm pitch grid

A method was developed of taking measurements from STM images, which showed that using this technique a high degree of repeatability was achievable (see Table 3.3). In addition the objectivity of this method minimises user subjectivity in the measurement process, which is essential for the optimum metrological use of this instrument. The calibration study itself indicated that there may be a problem with the derating procedure for scans in the $(80) \rightarrow (40\mu\text{m})^2$ scan ranges. The results also indicate that there was an overall error in measurements made of approximately 2%, which is the best estimate of the accuracy of measurements made with the STM using the procedures adopted in this work

These problems with the derating and instrument error could be minimised by systematically altering the derating and x, y sensitivity settings of the STM (see Section 2.1.3). However, unless an innovative method of optimising these parameters is proposed the only other alternative is by manually varying them by trial and error with a view to discovering optimum or adequate settings, which would prove tedious and would not guarantee success at the outcome

In summary, this study has illustrated both the strengths and weaknesses of using the STM as a metrological instrument. It must be understood that this study applies to only one commercial instrument, but that the methods employed to determine its metrological capabilities could readily be applied to other such instruments. For quick simple measurements at micron and sub-micron dimensions, with an accuracy of better than 5% the STM has few competitors

References.

- 1 G Reiss, J Vancea, H Wittmann, J Zweck, H Hoffmann , J Appl Phys 67(3) (1990) 1156
- 2 G Reiss, F Schneider, J Vancea, H Hoffmann , Appl Phys Lett 57(9) (1990) 867
- 3 J Tersoff, D R Hamann, Phys Rev Lett 50 (25) (1983) 1998
- 4 J Vancea, G Reiss, F Schneider, K Bauer, H Hoffmann, Surf Sci 218 (1989) 108
- 5 J E Griffith, D A Grigg, J Appl Phys , 74(9) (1993) R99
- 6 J A Stroci0, W J Kaiser, "Scanning Tunneling Microscopy", (Methods in Experimental Physics, Vol 27 , Academic Press, Inc 1993), Pg 4
- 7 P Moriarty, Report for National Metrology Lab , Forbairt, Dublin 9, Unpublished
- 8 "Guide to the expression of uncertainty in measurement", (International Organisation for Standardisation (ISO), Switzerland, 1995) Pg 66
- 9 "Guide to the expression of uncertainty in measurement", (International Organisation for Standardisation (ISO), Switzerland, 1995) Section 4.2.4

Chapter 4 : Scanning Tunnelling Spectroscopy of Gold in air

4.1 Introduction

This chapter deals with Scanning Tunnelling Spectroscopy(STS) studies of Au surfaces in both liquid and air environments. This was carried out in order to establish the validity of the STS technique under ambient conditions on an inert surface before studies of less stable semiconductor surfaces could be undertaken.

In the first part of the chapter the literature on experimental measurements of the apparent barrier height is reviewed. This is followed by a description of the calibration of the STM head used for the STS experiments and the STS measurements taken on Au surfaces .

4.2 Review of literature on Apparent Barrier Height.

This review includes how STS measurements in vacuum correspond with tunnelling theory. Then, how the model is modified for tunnelling in liquid or electrolytic environments in order to explain lower apparent barrier values measured under such conditions.

It was stated in section 1.3.2 that the apparent barrier height ϕ_b in STS is generally taken as the average of the tip and sample workfunctions. However, various groups have measured unusually low values for the apparent barrier height in air [1], liquids [2-4] and even under a moderate vacuum [5]. It is only under UHV conditions that values of the apparent barrier height close to what the theory would predict have been obtained [6-8].

Initial apparent barrier height measurements presented by Binnig and Rohrer[5] in their pioneering experiments using the STM on a platinum plate using a tungsten tip gave low values ($\phi_b \approx 0.6$ eV) under a moderate vacuum. It was only after cleaning the surface and under a vacuum of 10^{-6} Torr that a value ($\phi_b=3.2$ eV) closer to that predicted by theory was obtained. Later Gimzewski et al [6] measured values of $\phi_b=3.5$ eV on Ag and Kuk et al [7] measured a value of $\phi_b=3.4$ eV on Au, both under UHV conditions. Both these experiments report a drop off in the apparent barrier height as tip-sample contact is approached. Gimzewski et al [6] suggested that the collapse of ϕ_b at small tip-sample separations was due to the considerable overlap of

the electron densities of tip and sample at the Fermi-level Lang [9] provided a computational model to explain this drop off in ϕ_b (see Fig 4.1). In this he stated that it was not sufficient to compute the current for each electrode in the absence of the other because this approach was only appropriate when the separation of the electrodes is large and thus the overlap of the electrode wavefunctions is small. In the model the tunnel gap resistance was calculated to drop off exponentially as the tip approached the sample. However, about 3\AA from contact, the resistance remained constant as the tunnel gap decreased further. This effect was attributed to the atom at the tip apex representing a 'constriction' resistance, i.e. the tip atom presented a finite resistance such that reducing the gap further has little effect on the resistance of the tunnel gap.

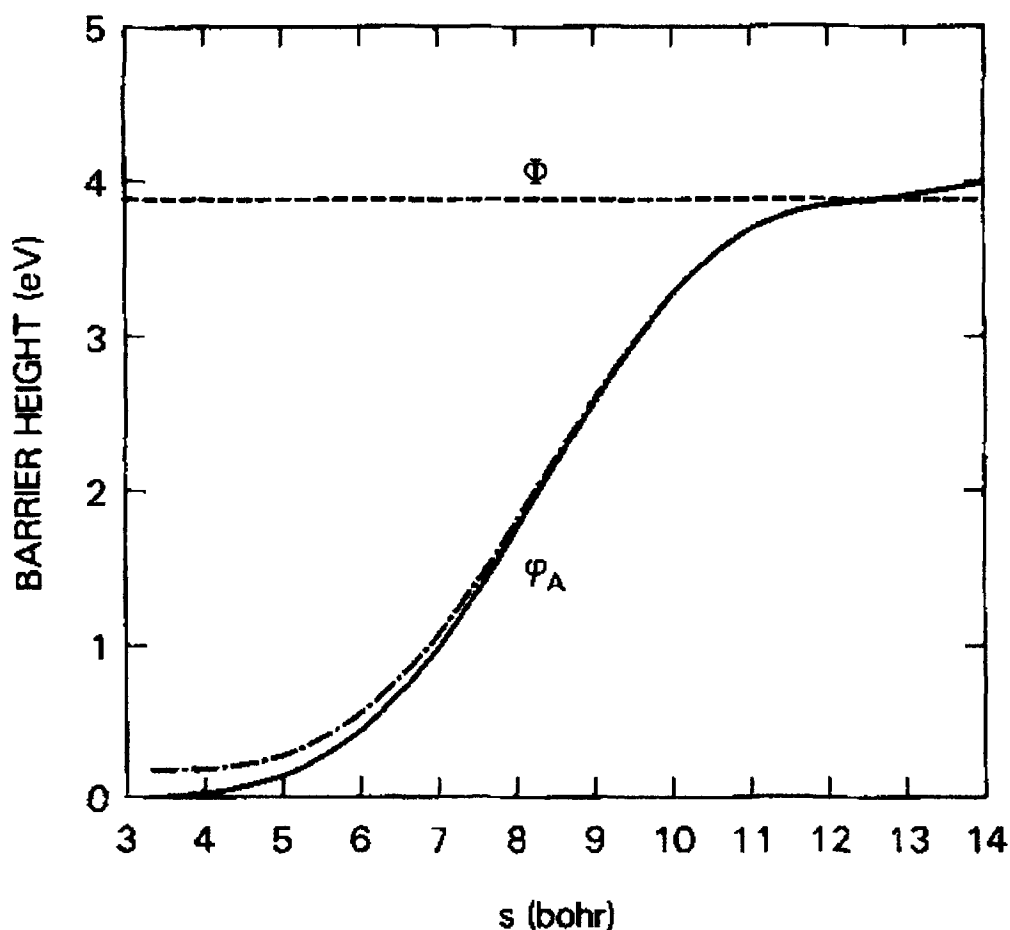


Fig 4.1 The variation in apparent barrier height with tip-sample separation (after Ref [9]). Φ is the average workfunction of the sample, ϕ_A is the apparent barrier height

This had the effect of reducing the expected exponential increase in tunnel current as the tip approached the sample

More recent measurements by Olesen et al [8] on the Au(110), Ni(100) and Pt(100) surfaces under UHV, values of $\phi_b = 4.7$ eV, 4.5 eV and 3.4 eV respectively, were obtained. However, they measured ϕ_b to be constant until point contact was established. They stated the reason for not seeing a fall off in ϕ_b as tip-sample contact was approached, was that the actual voltage across the junction (V_t) is not always equal to the applied bias (V_{bias}). V_t decreases as the tip-sample separation decreases due to the finite impedance of the current preamplifier, since V_{bias} is divided between this input impedance and V_t (which can be as low as 100Ω at close proximity [10]). This contradicts the earlier work of Gimzewski et al [6] and Lang [9] and suggests that the tunnelling process remains the dominant effect until tip-sample contact.

Measurements of the apparent barrier height in liquid environments, such as HClO₄ (10 mM), NaClO₄ (0.4 M), NaSO₄ (0.1 M) and decalin have yielded values of $\phi_b = 1 \rightarrow 2.15$ eV on Au(111) [2,3] and $\phi_b = 1.8$ eV on the Ag (100) surface imaged in NaClO₄ (0.5 M) [4]. These values are approximately 1–2 eV lower than values obtained in UHV environments. This has been attributed to a lowering of the potential energy barrier when in a solution [11]. Schmieder *et al* [11] proposed a model of tunnelling in an electrolytic environment. In the model it assumes that the transferring electron interacts with the polarisation of the solvent. It is suggested that the librational and vibrational modes of the solvent are slow compared with the speed of the tunnelling electron and therefore cannot respond to its transfer. Only the electronic polarisation, which gives rise to the optical dielectric constant ϵ_∞ , is sufficiently fast to respond to the electron's motion. The model shows that the effect of the solution is a lowering of the potential energy barrier due to the screening of the electrostatic interaction by ϵ_∞ , the optical dielectric constant. Using this model they calculated a drop of 1 eV in the barrier height between vacuum and electrolyte tunnelling. This effect was demonstrated experimentally by Pan *et al* [2] on the Au(111) surface in different electrolytic environments. Certain solutions provided permanent dipoles enhancing tunnelling from the substrate to tip and opposing tunnelling from the tip to substrate, thus demonstrating the effect of polarisation of the tunnel gap.

There is very little in the literature on ϕ_b measurements on metals in air. However, it has been suggested [1,5,12] that the contaminants present under non-UHV conditions are responsible for the low barrier height measurements.

4.3 Preparation of samples used.

The Highly Orientated Pyrolytic Graphite (HOPG) used in the lateral calibration is commercially available from Agar Scientific, Essex, UK. Immediately before imaging a clean surface was exposed by cleaving the sample.

The Au(111) surfaces used for the vertical calibration were prepared in a similar manner to that used by De Rose et al [13]. A freshly cleaved mica surface was heated in vacuum ($\approx 10^{-6}$ mbar) to 300°C during gold deposition. After a thick film of Au had been deposited, the surface was then annealed to 325-375 °C for 4-5 hours. This preparation is reported to produce single crystal facets of the Au(111) surface [2].

The Au(111) surfaces prepared on Si(100) were received from R. Rizza, Chemistry Dept. UCD. The Au layer was prepared by thermal evaporation at a rate of 1 Å per second to a final thickness of 600 Å. Prior to this the samples were annealed in air at 250 °C for three hours [14].

4.4 Calibration of small area scan head

The small area scan head for our STM has a maximum scan size of approximately $(700 \text{ nm})^2$ and is used mainly for achieving resolution down to the atomic scale. To calibrate this scan head laterally, HOPG was used as it has a lateral periodicity of 2.46 Å. Fig 4.2 shows an atomically resolved image of HOPG. The measured value of the pitch (from an average of 50 different pitch measurements) was 2.52 Å with a standard deviation of ± 0.29 Å. Using equation 3.6 for an uncertainty at 95% confidence we get the value of the pitch to be 2.52 Å with an error of 0.6 Å and an uncertainty in the measurement of 0.08 Å at 95% confidence.

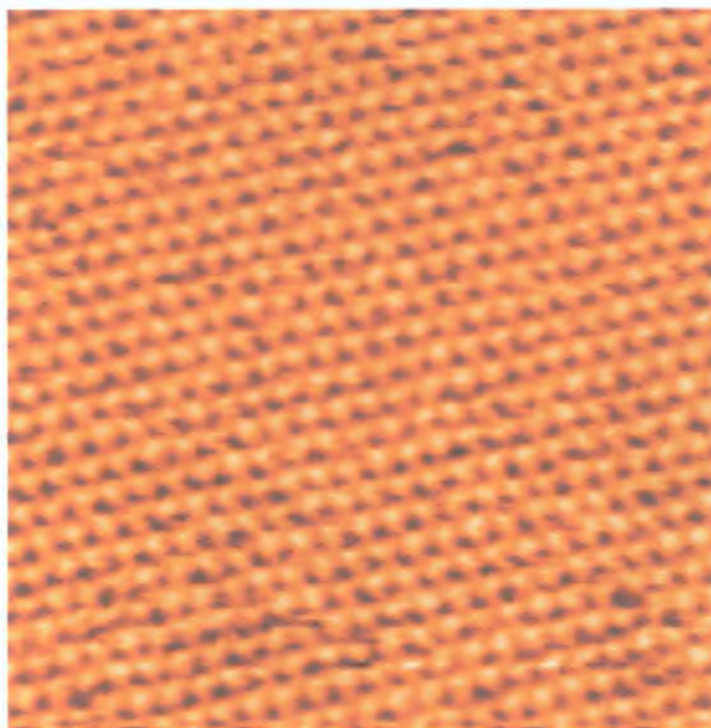


Fig 4.2. $(60.75 \text{ \AA})^2$ scan of HOPG

Atomic steps of the Au(111) surface were used to calibrate the scan head vertically. While atomic resolution was not quite achieved Fig 4.3 shows steps of the Au(111) surface at characteristic angles of 60° . The step height between planes of the atomically flat Au(111) surface is known to be 2.35 \AA . Fig 4.4 shows a profile of the image below and indicates the step heights of that particular profile.



Fig 4.3. $82 \times 50 \text{ nm}$ STM image of atomic steps on the Au(111) surface.

From profiles of this and other images of atomic steps the measured value for the atomic steps was 2.37 \AA with a standard deviation of 0.27 \AA . Again, using equation 3.6

to express a standard uncertainty at 95%, we can give the measured value for atomic steps on the Au(111) surface as 2.37\AA with an error of 0.2\AA and an uncertainty of 0.08\AA at a 95% confidence level.

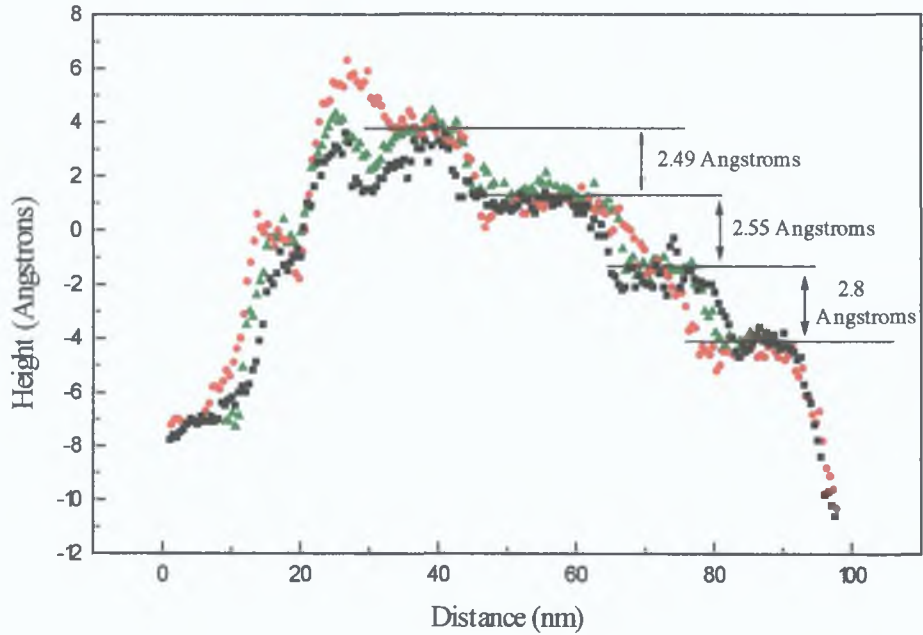


Fig 4.4. Profiles taken of stepped area of Fig 4.3. Measurements of the step heights are also shown.

4.5 Calculation of the apparent barrier height from experimental data.

As mentioned in section 1.3.2 in STS, the tunnel barrier (ϕ_b) can be extracted using the expression

$$\phi_b(eV) = 0.952 \left(\frac{d \ln I}{ds} \right)^2 \quad \dots (4.1)$$

where I is the tunnel current, and s is the tip-sample separation in Angstroms. Thus experimentally, from an (I-S) spectroscopic plot the apparent barrier height (ϕ_b) can be calculated by dividing the differential, dI/ds , by the current, I [15]. The dependence of tunnel current on relative separation is given by the fundamental expression,

$$I \propto \exp(-2 \chi \Delta s) \quad \dots (4.2)$$

where $\chi = \sqrt{2m\bar{\phi}}/\hbar$ and $\bar{\phi}$ is the mean workfunction.

Rewriting equation (4.2) as an equality we get,

$$I = k \exp(-2\chi\Delta s) \dots(4.3)$$

where k is the constant of proportionality.

thus differentiating the current, I with respect to the tip-sample separation, s we get ,

$$\frac{dI}{ds} = -2\chi k \exp(-2\chi\Delta s) = -2\chi I \dots(4.4)$$

substituting eqn(4.4) into eqn(4.1) this becomes,

$$\phi_b(eV) = 0.952\left(-\frac{2\chi I}{I}\right)^2 = 0.952(-2\chi)^2 \dots(4.5)$$

By fitting an exponential decay of the form of equation (4.2) to the spectroscopic (I-S) plots obtained, we could obtain a value for χ . Using this χ value, ϕ_b then can be calculated using equation (4.5).

Fig 4.5 shows a sample I-S spectroscopic plot with curve fit. It can be seen that the experimental data begins to deviate from the curve fit from $0 \rightarrow 1\text{\AA}$. This is not

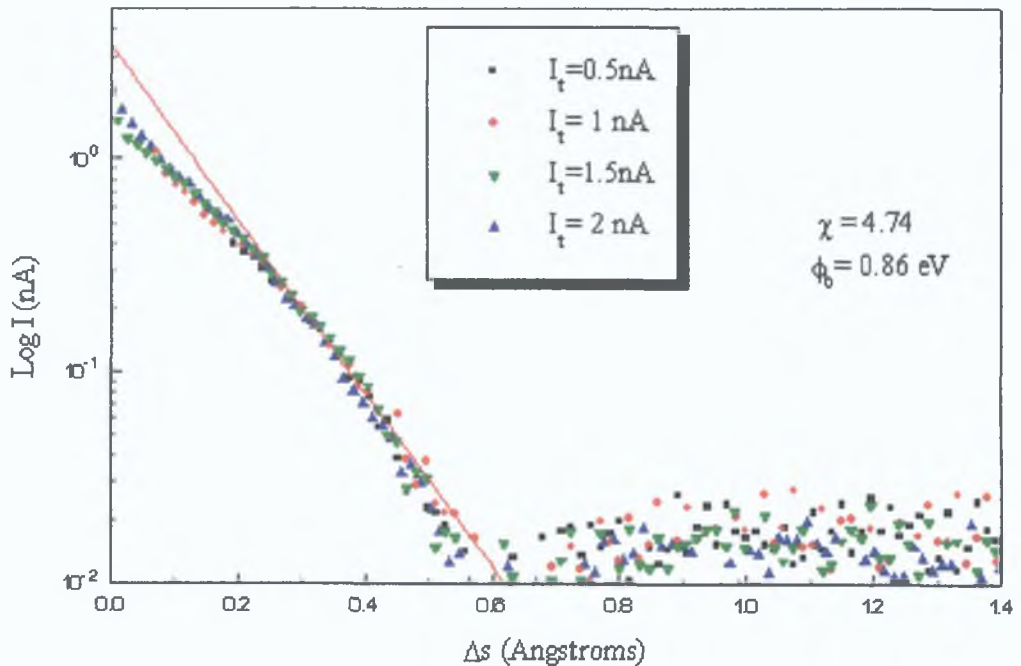


Fig 4.5. I-S spectroscopic plot of the Au(111) surface imaged in Air, at various tunnelling currents, I_t

surprising as the Nanoscope user manual warns that the reduced bias at higher tunnelling currents due to the preamplifier can cause the I-S plots to be inaccurate. This is similar to observation made by Olesen et al [8] , that the voltage across the tunnel gap is not always equal to the applied bias, particularly at low tip-sample separations. Were this not taken this into consideration a drop off in ϕ_b at small tip-sample separations would be observed, similar to the findings of earlier groups [6,7]. In order to avoid this problem we generally used low setpoint currents of 1 nA.

4.6 Scanning Tunnelling Spectroscopy of the Au(111) surface.

4.6.1 I-V spectroscopy.

In order to establish that the spectroscopic facility was operating correctly I-V spectroscopy was initially carried on the Au(111) surfaces. Fig 4.6. shows typical plots obtained for the samples. The curves are characteristic for metals and show the exponential increase with increasing applied bias as predicted in section 1.3.1.

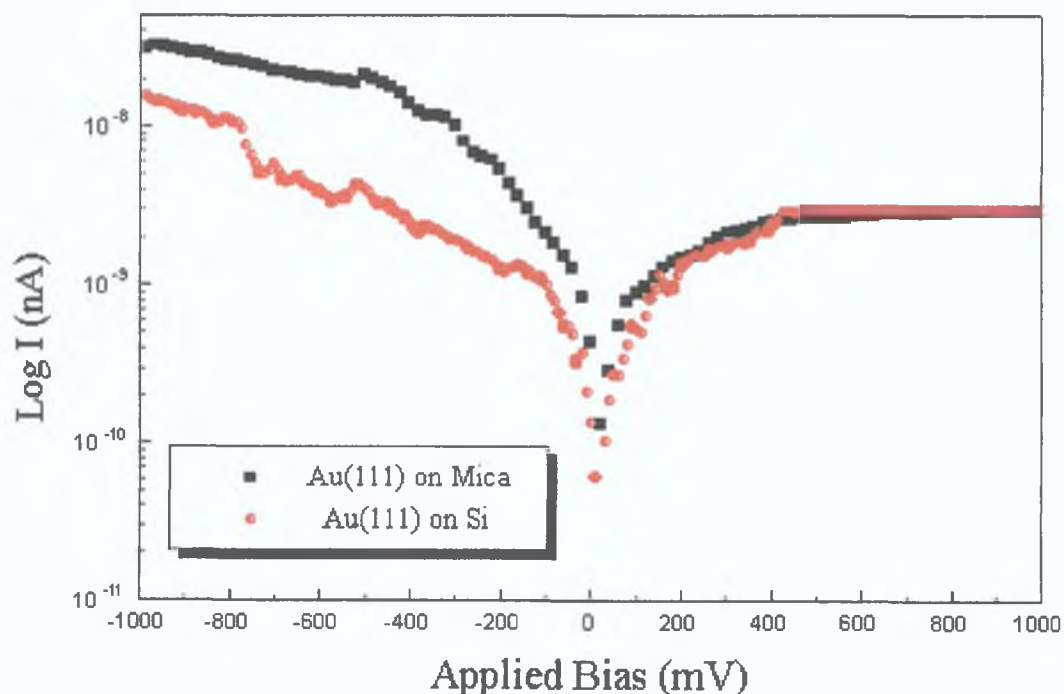


Fig 4.6. Typical I-V curves for Au(111) surfaces.

4.6.2 I-S spectroscopy

In order to validate the I-S spectroscopic capabilities measurements of our STM we first imaged the Au(111) surface in decalin. decalin ($C_{10}H_{18}$) is a nonpolar liquid of low polarisability, which was used by Pan et al [2] to investigate the effect of polarisation of the tunnelling medium on the measured apparent barrier height. Imaging the Au(111) surface in decalin with a Pt-Ir tip, Pan et al [2] measured an apparent barrier height of 1.52 ± 0.3 eV.

Fig 4.7. shows a typical I-S curve, with curve fit, obtained for the Au(111) surface in decalin imaged using a Pt-Ir tip. The applied bias was $V_b=20$ mV and the setpoint current was $I_t = 3$ nA. Several measurements were made at a range of V_b at both positive and negative biases as seen from Fig 4.8. Averaging these, we obtained a value of $\phi_b = 1.4 \pm 0.24$ eV. This is close to the value obtained by Pan et al [2]. An important aspect of Fig 4.8 is that there is no dependence of the calculated ϕ_b on the voltage polarity. It is significant that we do not see a noticeable difference between the measured barrier height values at positive and negative bias values for results obtained in decalin. This runs contrary to the findings of Pan et al [2], yet it was the result Pan et al. had predicted because, as mentioned earlier, decalin is a nonpolar liquid.

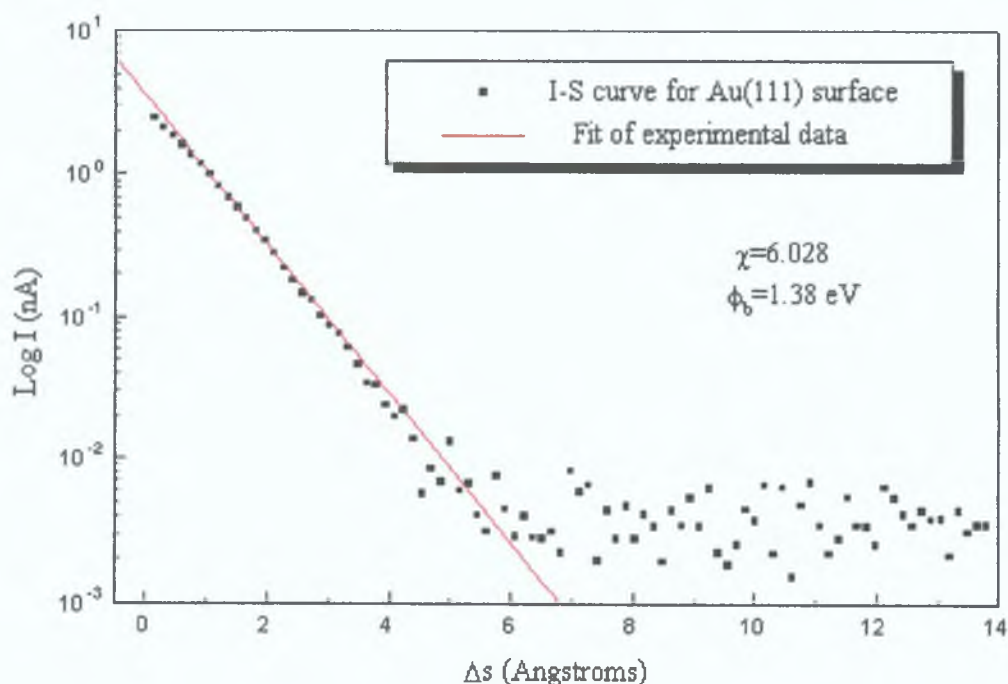


Fig 4.7. I-S spectroscopic plot of the Au(111) surface imaged in Decalin.

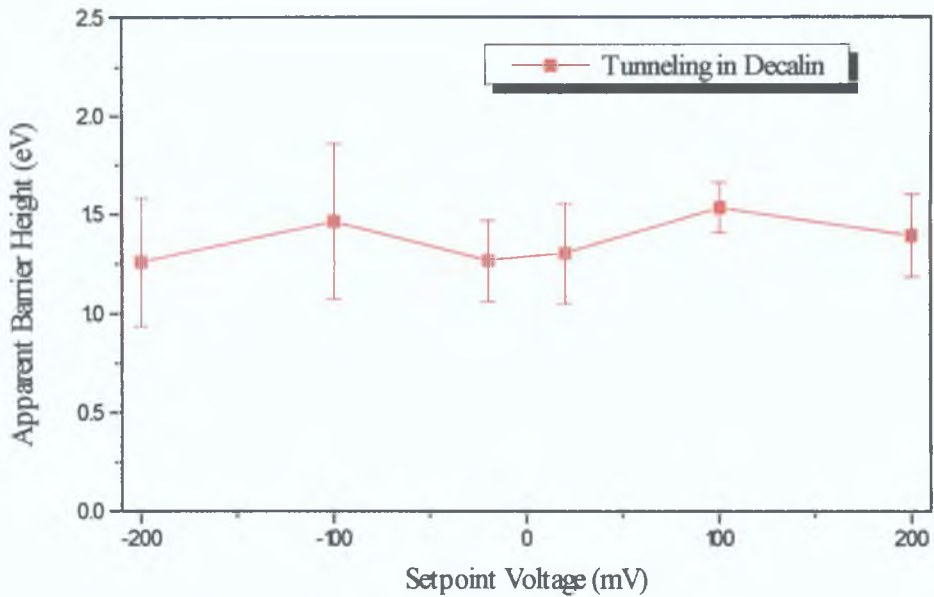


Fig 4.8. Variation in apparent barrier height with applied bias (V_b)

I-S spectroscopy for the same Au(111) surface in air gave an average value of $\phi_b = 1.02 \pm 0.22$ eV, which is lower than the value obtained in decalin. The barrier heights measured in air are generally lower than those in decalin. Considering the contaminants present under ambient conditions plus the constantly changing nature of the tunnel gap in air, this value is considered to be a reasonable estimate value of ϕ_b for the Au(111) surface in air.

It was shown above how the measured barrier height for the Au(111) surface imaged in decalin was independent of the voltage polarity. However, measurements in air for the Au(111) surface prepared on two different substrates, display considerable differences between the measured barrier height values at positive and negative biases, as shown in Fig 4.9. The picture presented by Fig 4.9 may be explained by considering there to be fixed polarisation of the tunnel gap. Fig 4.10 shows schematically the tunnelling electron interacting with a fixed polarisation gap [2]. For the direction of polarisation shown, at negative sample bias the polarisation of the gap assists the tunnelling electron as suggested by Schmickler et al [11]. This results in a slower fall

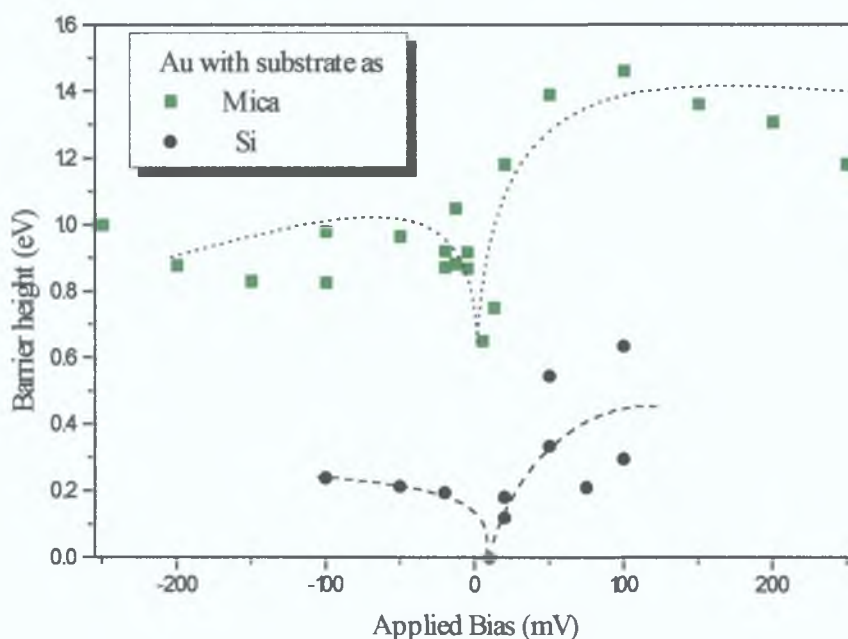


Fig 4.9. Variation in barrier height with applied bias for Au(111) prepared on Si and Mica substrates. Samples imaged in air. (Note: Dashed lines are only a guide).

off in tunnel current with increasing tip-sample separation, hence the lower barrier height, similar to that in Fig 4.9. At positive bias the polarisation of the tunnel gap shown in Fig 4.10 hinders the tunnelling electron. This results in an increase in the fall off in tunnel current as the tip sample separation increases.

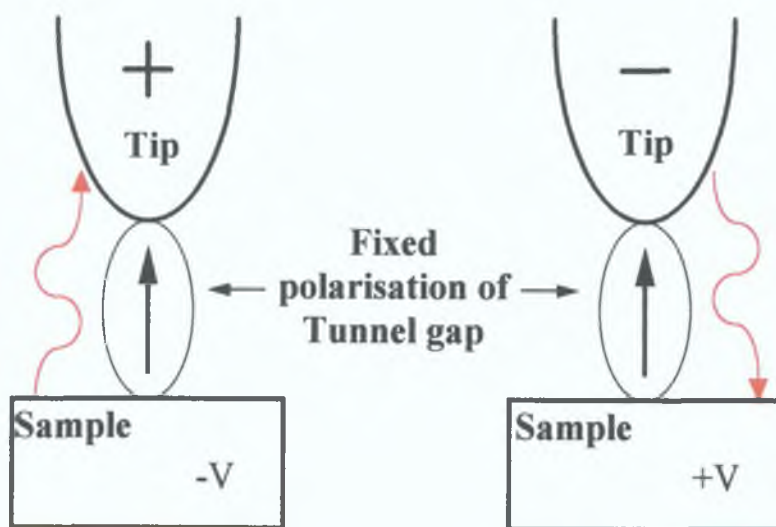


Fig 4.10. Sketch of how fixed polarisation of the tunnel gap affects tunnelling at positive and negative sample bias.

Thus, in this case a higher barrier height is measured, as is the case for the values measured at positive bias in Fig 4.9.

The other item of interest in Fig 4.9 is that the barrier height measurements for the Au(111) surface prepared on Si substrates are considerably lower than those for the same surface prepared on mica. The average for Au(111) surface prepared on Si was $\phi_b = 0.3 \pm 0.16$ eV. It was noticed that images of the Au(111) surface prepared on Si did not appear as smooth as those of the same surface prepared on Mica, so the variation in barrier height with root mean square roughness was plotted (see Fig 4.11) to see if there was any indication that surface roughness could perhaps affect the barrier height measurements.

It can be seen that the data in Fig 4.11 is well scattered about the fit line, so although not conclusive, the trend suggested by the data is that the barrier height measurement does seem to be lower for rougher surfaces. This can be explained by comparing the tip-sample geometry of the case for a smooth and a rough surface [16]. As can be seen from Fig 4.12 a vertical modulation of the tip, Δz via the piezoelectric holder, does not necessarily mean that the tip-sample separation, Δs has been

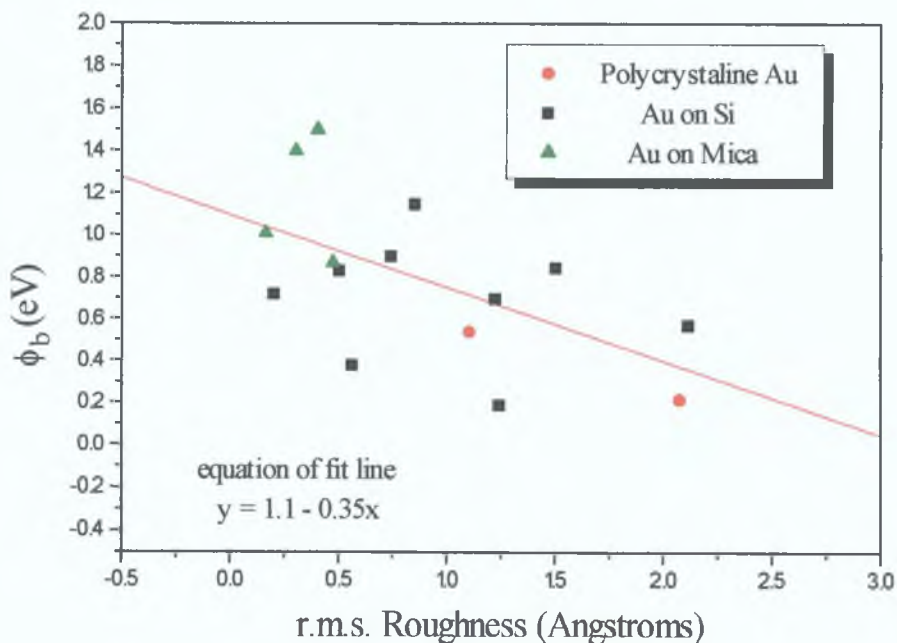


Fig 4.11. Variation in apparent barrier height with surface roughness for various Au surfaces.

modulated by the same amount. In fact $\Delta s = \Delta z$ only if the z-direction coincides with the direction of the surface normal to the tip, as in Fig 4.12(a). Otherwise there is an angle, ϕ between these two directions as in Fig 4.12(b).

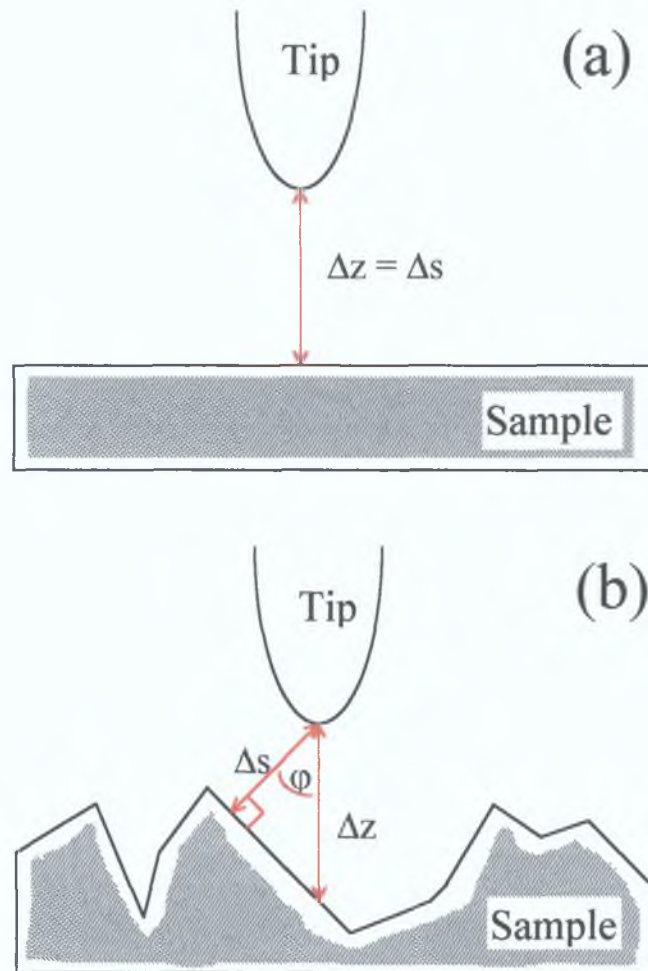


Fig 4.12 Sketch showing effect of (a) smooth and (b) rough surface can have on I-S spectroscopy.

Thus we can write the actual tip-sample separation, Δs in terms of the tip modulation, Δz in,

$$\Delta s = \Delta z \cdot \cos(\phi) \dots (4.6)$$

$$\text{thus } \frac{\Delta \ln I}{\Delta s} = \frac{1}{\cos(\phi)} \cdot \frac{\Delta \ln I}{\Delta z} \dots (4.7) \text{ and letting } \frac{\Delta \ln I}{\Delta s} \approx \frac{d \ln I}{ds} \dots (4.8)$$

but we measure the barrier height from equation 4.1 as

$$\phi_n (\text{eV}) = 0.952 \left(\frac{d \ln I}{dz} \right)^2 \dots (4.9)$$

whereas the true barrier height for the material, ϕ_b , is given by

$$\phi_b (eV) = 0.952 \left(\frac{d \ln I}{ds} \right)^2 \quad (4.10)$$

rearranging equation 4.7 and substituting into the equation for the measured barrier height, ϕ_m , equation 4.9 we get,

$$\phi_m = 0.952 \left(\cos(\varphi) \frac{\Delta \ln I}{\Delta s} \right)^2 = \phi_b \cos^2(\varphi) \quad (4.11)$$

We see from equation 4.11 that the effect in of the rough surface is to reduce the measured barrier height by a factor of cosine of the angle between the surface normal and the z-direction squared, from the actual barrier height

4.7 Conclusions

In this chapter we have documented the calibration of the small scan head for the Nanscope II both laterally and vertically. Characteristic I-V curves were obtained for the Au(111) surface. We measured values of the barrier height of the Au(111) surface under decalm to be 1.4 ± 0.24 eV, which is close to the value previously reported [2]. The value of the barrier height for the same Au(111) surface in air gave a slightly lower value. This was deemed to be due to the contaminants present in air and polarisation of the tunnel gap, but was considered to be a reasonable value for the barrier height under ambient conditions.

Other factors influencing the barrier height measurement were touched upon also, including the effects of measuring the barrier height at different applied biases and the effect of surface roughness on the barrier height. The most significant effect of measuring the barrier height at different applied biases seemed to be that the state of polarisation of the tunnel gap could be inferred. The surface roughness seemed to be a factor in the measured value of the barrier height. However, a more extensive study would need to be carried out in order to determine this fact conclusively and perhaps quantify the extent to which the barrier height is affected by the surface roughness comparing experimental data with the model described.

The results discussed above show that the main objective of this chapter, which was to understand the I-S spectroscopic technique under ambient conditions, was

achieved It was also shown that I-S spectroscopy provides a quantitative indicator of the interaction present at the tip-sample gap This is an advantage that I-V spectroscopy, though it can provide a characteristic curve for different conductors, does not have

References.

- 1 H J Mamin, E Ganz , D W Abraham , R E Thomson , J Clarke , Phys Rev B 34(12) (1986) 9015
- 2 J Pan, T W Jing, S M Linsay , J Phys Chem ,92 (1994) 5563
- 3 J Wiechers, T Twomey, D M Klob, J Electroanal Chem , 248 (1988) 451
- 4 R Christoph, H Siegenthaler, H Roher, H Wiese, Electrochimica Acta, 8 (1989) 1011
- 5 G Binnig , H Roher , Ch Gerber , E Wiebel , Appl Phys Lett 40(2) (1982) 178
- 6 J K Gimzewski, R Moller, Phys Rev B, 36(2) (1987) 1284
- 7 Y Kuk and P J Silverman, J Vac Sci Technol A 8(1) (1990) 289
- 8 L Olesen, M Brandbyge, M R Sørensen, K W Jacobson, E Lægsgaard, I Stenegaard, F Besenbacher, Phys Rev Lett 76(9) (1996) 1485
- 9 N Lang , Phys Rev B 36(15) (1987) 8173
- 10 M Brandbyge, J Schiøtz, M R Sørensen, P Stoltze, K W Jacobson, J K Nørskov, L Olesen, E Lægsgaard, I Stenegaard, F Besenbacher, Phys Rev B 52 (1995) 8499
- 11 W Schmiedler, D Henderson, J Electroanal Chem , 290 (1990) 283
- 12 J H Coombs, J K Pethica, IBM J Res Dev 30(5) (1986) 456
- 13 J A DeRose, D B Lampner, S M Linsay , J Vac Sci Technol A 11(4) (1993) 776
- 14 R Rizza, D Fitzmaurice, S Hearne, G Hughes, G Sporto, E Ciliberto, (Unpublished)
- 15 C J Chen , R J Hamers , J Vac Sci Technol B 9(2) (1991) 503
- 16 R Weisendanger “ Scanning Probe Microscopy and Spectroscopy”, (Cambridge University Press, 1994) Pg 139

Chapter 5 : STM/S of Sulphur Passivated InP

5.1 Introduction

In this chapter, we present the results of current-voltage (I-V) and current-distance(I-S) characterisation studies of wet chemical sulphur passivated InP(100) surfaces. The aim of the study was to attempt to establish a more quantitative measure of the surface passivation characteristics. The reproducibility and reliability of (I-S) data was established from preliminary measurements made on a Au(111) surface, as discussed in Chapter 4. This allowed the validity of measurements which were subsequently made on the passivated InP(100) surface to be assessed. The chemical composition of the InP(100) surface before and after sulphur passivation is determined by x-ray photoelectron spectroscopy (XPS) measurements .

5.2 Passivation of semiconductor surfaces.

The atoms in solids are geometrically structured such that the net force acting upon each atom is zero. However, at the surface there will be differences in the structure from that prevailing in the bulk. This arises due to the absence of neighbouring atoms which means that the equilibrium positions of the surface atoms will differ from those in the bulk. The result is either a relaxation or reconstruction of the surface atoms. A relaxation means that the surface will retain the bulk symmetry but the spacing of the surface atoms will be different in the direction perpendicular to the bulk. If there is a reconstruction of the surface the atoms rearrange such that the symmetry differs from that of the bulk. The chemical nature of the surface may also differ from the bulk . Atomically clean surfaces can only be generated under certain ideal conditions, such as cleavage of a sample under Ultra High Vacuum (UHV) conditions. Cleavage of a sample under normal atmospheric conditions will lead to an adsorbed layer of atoms from the surrounding environment forming almost instantaneously .

The surfaces of solids therefore are complex regions with a different chemistry and crystallography from the bulk. It is understandable that the electronic states at the surface will differ from those of the bulk.

Consider the surface of a semiconductor as the bulk periodic potential is abruptly terminated. The conditions which give rise to the forbidden energy gap (or band gap) in the bulk may no longer prevail at the surface. In fact it is often the case that at the surface there will be electronic states within the band gap.

To look at the effects of the surface states on the energy level diagrams for a semiconductor, we first define a neutral level, ϕ_0 , for an electrically neutral surface which corresponds to an effective Fermi level. Consider a semiconductor surface which has surface states such that the filled states lie within the bulk valence band and the empty states were in the bulk band gap (as is the case for the clean, cleaved, $\text{Si}(2 \times 1)$ reconstructed surface [1]). For this case ϕ_0 would lie between the empty and filled surface states. In the event that the effective surface Fermi level, ϕ_0 did not correspond to the bulk Fermi level, a net charge will reside at the surface. This will create an electric field in the semiconductor which will affect the energy bands at the surface and lead to “band bending”, as in Fig 5.1. For an n-type semiconductor the bands bend upward for a net negative charge and downward for a net positive charge.

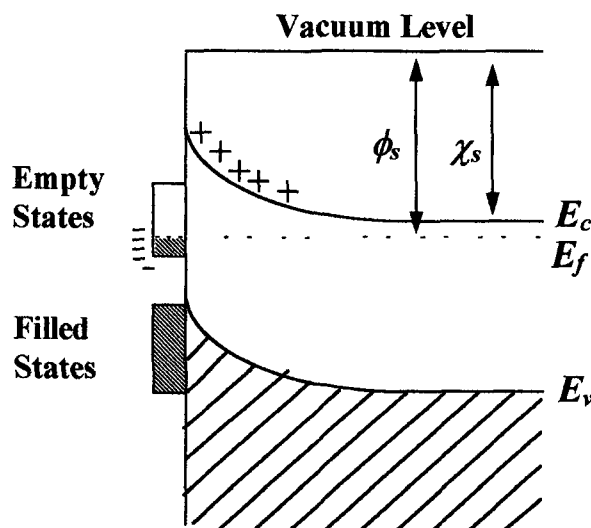


Fig 5.1 Surface state induced band bending in a semiconductor

In order to understand the concept of Fermi level pinning let us first consider metal-semiconductor contacts and Schottky barriers. Consider a semiconductor with no surface states present (flat band condition) as in Fig 5.2(a). If a metal is brought into contact with this semiconductor surface there will be a transfer of charge between the two, such that the two Fermi levels coincide in equilibrium (as in Fig 5.2(b)). For an n-type semiconductor this would involve a transfer of electrons from the

semiconductor into the metal. Thus positive charge due to uncompensated donors will reside in the near surface region which has been depleted of electrons giving rise to the band bending at the semiconductor surface. In this equilibrium position the energy barrier, ϕ_b , to electrons going from the metal into the semiconductor is given by the expression

$$\phi_b = \phi_m - \chi_s \quad (5.1)$$

where ϕ_m is the metal workfunction and χ_s is the semiconductor electron affinity. The energy barrier, ϕ_b is known as the Schottky barrier. This model suggests a linear relationship between the metal workfunction and the Schottky barrier.

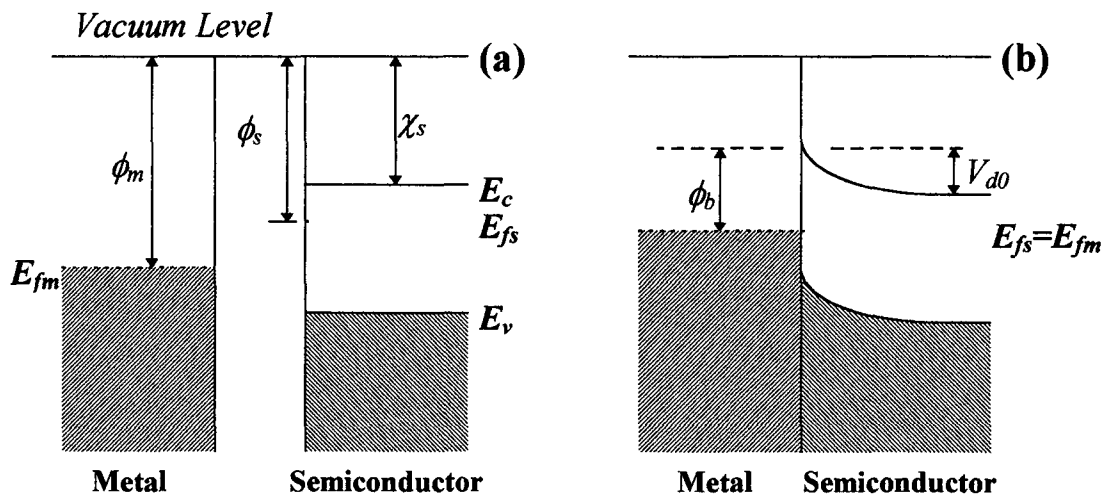


Fig 5.2 Formation of a Schottky barrier between a metal and an n-type semiconductor (a) metal and semiconductor separated (b) Metal and semiconductor in contact

However, experimental work indicated that ϕ_b was not as sensitive to ϕ_m as the Schottky model suggests, and in some cases independent of ϕ_m . Bardeen [2] suggested a reason for this. He proposed that in the presence of sufficient density of intrinsic surface states, following the deposition of a metal onto the semiconductor surface, the charge transfer at the interface will be effectively between the surface states and the metal. Thus the interior of the semiconductor is effectively screened from the metal by these surface states. In this case the Fermi level is said to be effectively pinned by the surface states and the Schottky barrier becomes independent of the metal workfunction.

Fermi level pinning has obvious implications for the engineering of Schottky barriers of required energies in device applications. For this reason there is considerable interest in the preparation of surfaces that reduce surface state densities, decrease the band bending and unpin the Fermi level. Deposition of a passivating adsorbate layer on semiconductor surfaces has demonstrated its potential in achieving these goals [3,4]

5.3 Literature Review

There have been a number of studies which have used scanning tunnelling spectroscopy to characterise the passivated surfaces of GaAs [5-11] and InP[12] under ambient conditions. The main thrust of these studies has been to determine the topographic uniformity of the passivated surfaces and the determination of the resistance of these surfaces to ambient oxidation. Ha et al [5] have investigated the correlation between the surface morphology and the chemical composition while Nozaki *et al* [7] focused on the differences in the topographic images obtained by scanning the passivated surfaces with STM and atomic force microscopy (AFM). A comprehensive analysis of the $P_2S_5/(NH_4)_2S$ treated GaAs(100) surface has been carried out by Dagata et al [8-10] with the objective of preparing a surface which is both topographically and chemically uniform and suitable for subsequent processing. The STM is an ideal instrument to determine this information as the image contains information on both the surface topography and local electrical conductivity. Changes in the local conductivity due, for example, to the presence of poorly conducting oxide regions would appear as variations in the surface topography due to the movement of the STM tip towards the surface in order to maintain a constant tunnel current. Variations in the STM surface profile are therefore a critical measurement of the surface topography and chemical uniformity. Kurihara et al [12] have reported that the STM image of a unpassivated InP surface appears rough while the image of the same surface coated in a metal overlayer appears smooth. This they interpret as evidence that the surface roughness observed on the untreated surface is due to chemical inhomogeneities rather than topographic nonuniformities.

More recently, Silver et al [13] have investigated the application of scanning tunnelling spectroscopy to the characterisation of passivated GaAs(110) surfaces in air and in vacuum. These measurements allow spectroscopic information over a range of bias voltages to be acquired which provides information on the distribution of electronic states in the semiconductor band gap region. These are therefore less prone to the possibility of features appearing in the STM image as a consequence of scanning the semiconductor surface at a fixed bias. They reported systematic differences in the spectroscopic plots for the same surface imaged both in air and vacuum. They speculated that this could be due to the dielectric breakdown of polar contaminants adsorbed on the samples imaged in air. In general, the acquisition of STM images of passivated surfaces under ambient conditions presents a number of inherent problems. Firstly, the passivated surfaces are almost always unstable with respect to prolonged exposure to ambient conditions, especially those surfaces terminated in only a monolayer of passivating sulphur. Secondly, it has previously been shown that the very process of scanning the surface can result in enhanced local oxidation in the scanned region [11]. Nevertheless, the development of a method which allows for a simple rapid quantitative assessment in air of the passivation characteristics of these surfaces is of importance especially as it is compatible with the conventional conditions under which the wet chemical passivation treatments are undertaken.

The wet chemically sulphur passivated InP(100) surface has been shown to exhibit a highly stable (1x1) surface [14] reconstruction consisting of the surface being terminated in a monolayer coverage of sulphur atoms bridge bonded to surface Indium atoms. Tao et al [14] reported that it was possible to obtain a (1x1) LEED pattern on this passivated surface even after three days exposure to air. The (1x1) surface reconstruction transforms to a (2x1) reconstruction following annealing above 350 °C [15]. Mitchel et al [15] reported that there was an absence of electronic states at the Fermi level from combined photoemission and inverse photoemission studies of the (2x1) sulphur terminated surface. This suggests that the Fermi level was unpinned at the surface and indicated that the surface was effectively electronically passivated.

The stability of this passivated surface makes it a suitable candidate for an attempted ambient based characterisation method to assess the electronic state of the surface .

5.4 XPS study of InP

Fig 5.3 shows the XPS data taken from both untreated and S-passivated InP . The cleanliness of the S passivated InP is clear , since the relative intensity of the C 1s peak decreases , as does the O 1s peak . The substantial increase in the ratio of the In 3d

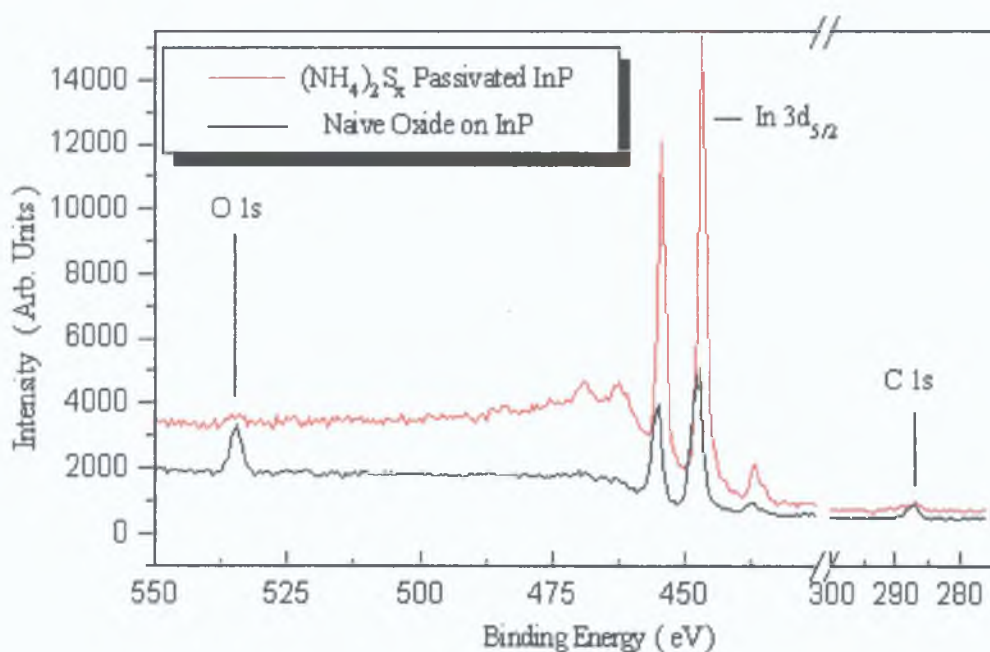


Fig 5.3. Survey XPS spectra of native oxide and sulphur treated InP, showing the drop in intensity of the Carbon and Oxygen signals prior to sulphur treatment.

peaks to the carbon and oxygen peaks verifies this further . The carbon peak at 284 eV suggests physisorbed carbons [16] .The XPS scan of the P 2p (Fig 5.4) peak on the untreated surface shows the expected P 2p peak for InP at 128 eV [16] , along with an oxide peak at 132.7 eV . On the S passivated surface the P 2p peak is again at 128 eV, with no discernible oxide peak present . A weak (1x1) LEED pattern was observable on the passivated surface .

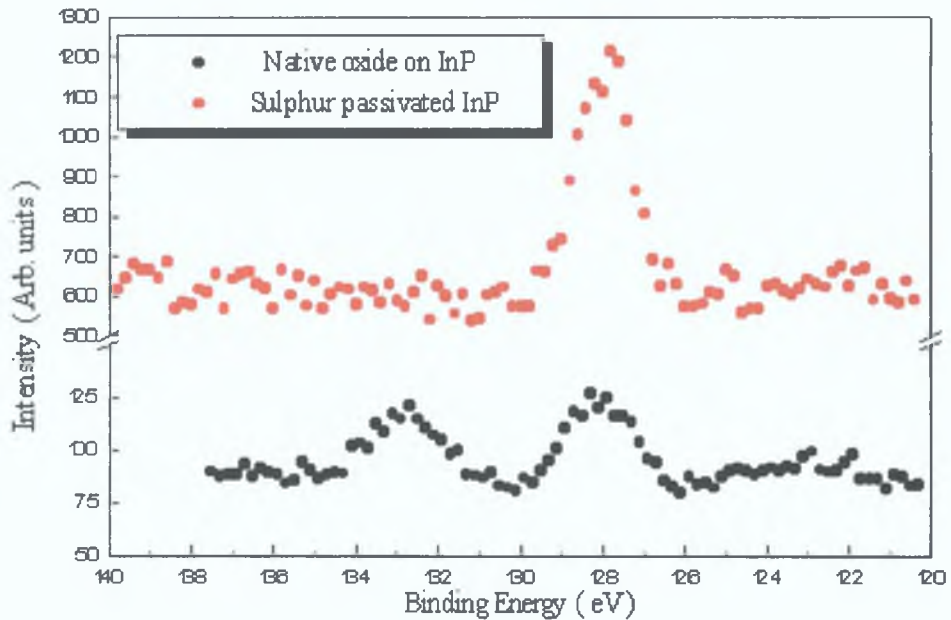


Fig 5.4. XPS spectra of the Phosphorus 2p peak for the native oxide and sulphur treated InP samples.

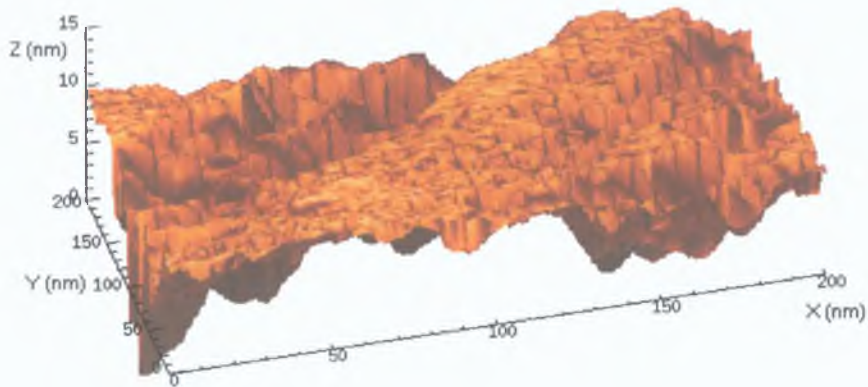
The XPS and LEED studies indicate that the passivation treatment used was effective in removing the native oxide from the InP (100) surface and replacing it by an ordered surface terminated layer as has been previously reported .

5.5 Surface Roughness.

The Nanoscope software allows the root mean square (rms) roughness for a defined area of a surface be calculated. This calculation is described in appendix A.

An STM image of the untreated InP (see Fig 5.5) surface had an r.m.s surface roughness value of ~ 6.5 nm for an area of 200 nm^2 , which is indicative of an oxide contaminated surface[11,12], while images taken of the S-passivated surface had an r.m.s. roughnessvalue of ~ 0.5 nm, over the same area . This corresponds with the findings of Kurihara *et al* [12] on the InP surface.

STM image of Native Oxide of InP(100)



STM image of Sulphur Passivated InP(100)

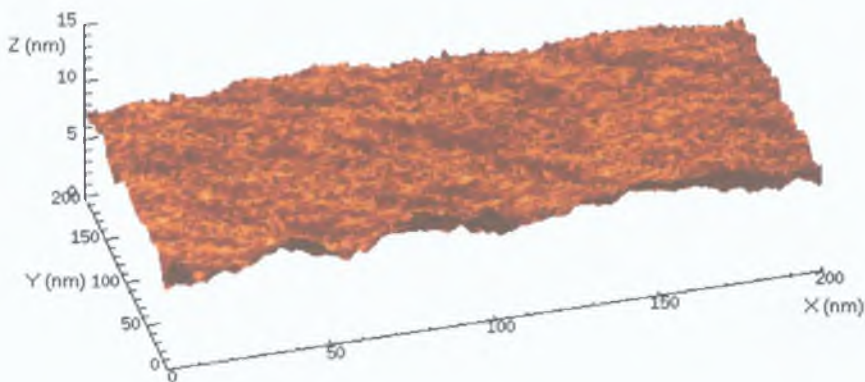


Fig 5.5. 3-D plots of STM images of the native oxide and sulphur passivated InP surface.

5.6 I-V spectroscopy

A sample I-V plot of the untreated surface is shown in Fig 5.6, see outer curve. A gap can be seen in the I-V curve where the detected tunnel current is low, from - 1.1 to +0.2 mV. Similar I-V curves were observed on n-GaAs in air [13], and O-terminated GaAs in vacuum [17]. The inner I-V plot taken on an S-passivated surface and is characteristic for a heavily doped semiconductor [17], in that three components of the tunnelling current are present. At large negative voltages we observe tunnelling out of the valence band (from -2 V \rightarrow -1.1 V - indicated by **V** in Fig 5.6). Similarly at positive voltages, tunnelling occurs into empty conduction band states above the Fermi level (indicated by **C** in Fig 5.6).

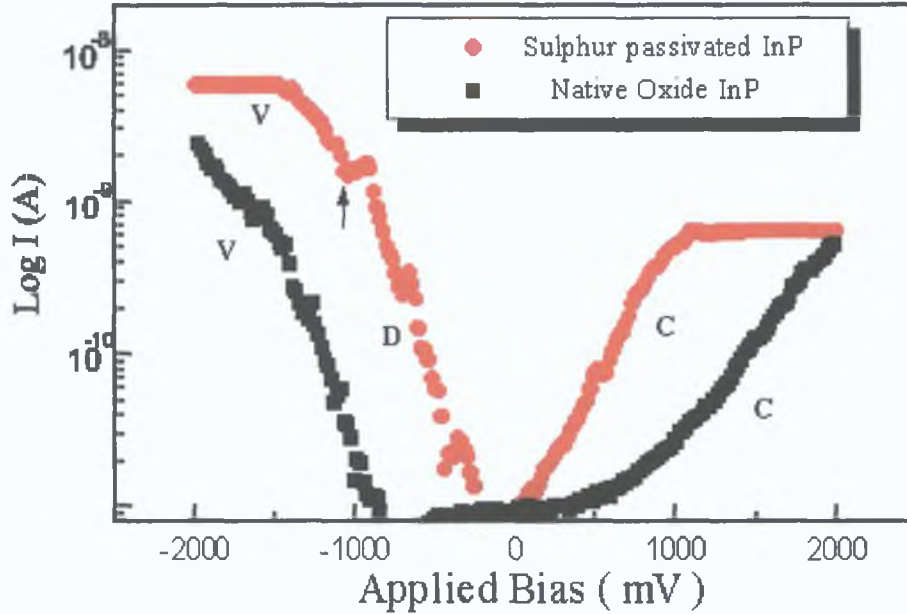


Fig 5.6. I-V spectroscopic plots for the native oxide and sulphur passivated InP.

Since there should be no surface states in the band gap for passivated InP tunnelling observed at small negative biases, between -1.1 and 0 V, is due to tunnelling out of conduction band states, as these states are occupied because of the heavy *n*-type doping. For an intrinsic semiconductor no significant tunnel current would be expected at low positive and negative voltages (i.e. $\pm qV < 1/2 E_{g_i}$, where q is the charge on an electron and E_{g_i} is the band gap energy).

Strocio *et al* [17] found that for oxygen adsorbed on a heavily *n*-doped GaAs surface a gap, similar to that for the native oxide curve in Fig 5.6, opened up in the I-V characteristic curve. The formation of this gap was associated with defect-induced band bending at the semiconductor surface, which effectively pinches off the dopant-induced tunnelling component. We conclude that the oxides on the untreated surface result in band bending, and hence the I-V characteristic curve as in Fig 5.6.

As mentioned earlier, the process of scanning the surface has been shown to result in enhanced local oxidation of the scanned region [9,11]. Although scanning the S-passivated surface did not produce any noticeable change in the surface, the I-V spectroscopy did appear to induce local oxidation of the surface. This can be seen in the

Fig 5.7, where we see the I-V curves change from the expected curve for a passivated surface, to that expected for an unpassivated surface, after only a few scans.

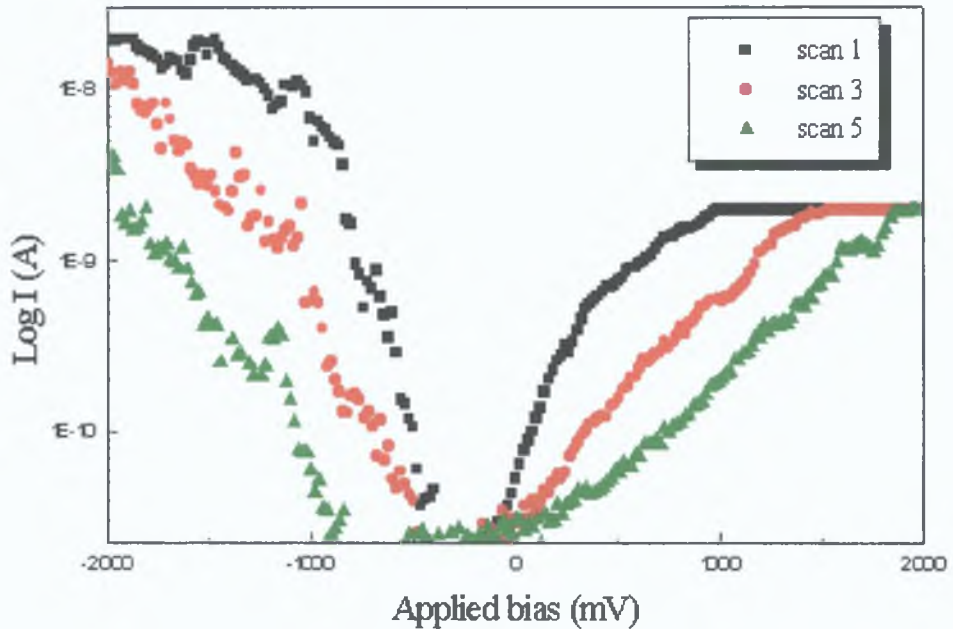
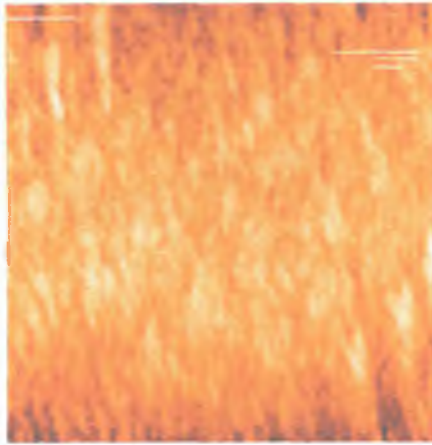


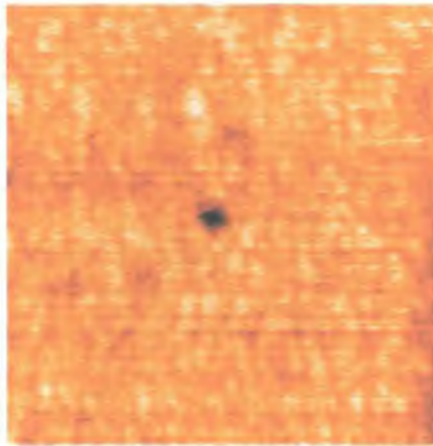
Fig 5.7 Variation in subsequent I-V plots taken on sulphur passivated InP.

The locally ‘damaged’ areas, due to I-V spectroscopy, could be seen in subsequent images taken of the surface (as in Fig 5.8). Further I-V spectroscopy carried out on the surface within 100 → 200 nm of the initially damaged area, on areas of the surface which appeared unchanged from the original scans taken of the surface, yielded I-V curves that had bandgaps of ~700→800 mV. This may indicate that the spectroscopic induced damage has resulted in localised band bending of the surface energy levels.

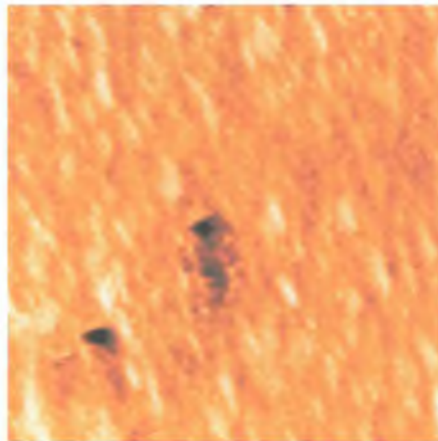
The I-V spectroscopic results illustrate that the surface electronic characteristics are altered by the very mechanism of acquiring the data. This inherent instability makes it impossible to efficiently use this method as an effective way of assessing the surface electrical characteristics.



(a) 300 nm² scan.



(b) 300 nm² scan



(c) 300 nm² scan.

Fig 5.8 STM images of sulphur passivated InP (a) before I-V spectroscopy, (b) after I-V spectroscopy and (c) after second set of I-V spectroscopic measurements after tip had been moved to top right of previous image.

5.7 I-S spectroscopy

The (I-S) spectroscopic plots for the gold reference in air and the passivated and unpassivated surfaces are shown in Fig 5.9. It is immediately apparent from the figure that the gradients of the (I-S) graphs, from which the barrier heights are calculated, differ significantly. A barrier height value for the untreated InP surface of approx. 0.3 ± 0.1 eV was obtained at an applied bias of -1600 mV. However, on passivated surfaces, again with $V_b = -1600$ mV, values of 0.054 ± 0.018 eV has been obtained for ϕ_b . These values for the barrier height are approximately an order of magnitude lower than those obtained on untreated surfaces. We attribute the lower barrier height, on

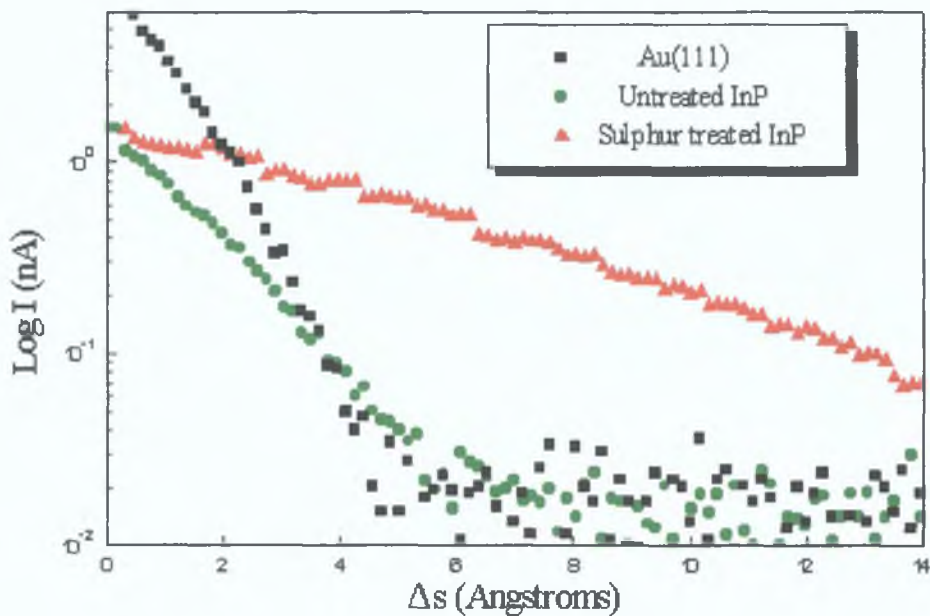


Fig 5.9. I-S curves of the Au(111), Native oxide of InP and S passivated InP

the passivated surfaces to the slower fall-off of current with distance, which is expected for an unpinned semiconductor surface. This has been attributed by Weimer *et al* [18] to two opposing effects which become apparent on an unpinned semiconductor surface. The first effect is the expected exponential fall-off in tunnel current with increasing tip-sample separation. The second effect is tip-induced band bending of the energy levels at the semiconductor surface. The tip-induced band bending increases the width of the depletion layer in the semiconductor such that electrons have to tunnel first through the depletion layer and then through the gap separating tip and sample. As the tip was

withdrawn the effect of this tip-induced band bending decreased, and thus the depletion layer width also decreases. The effect of the decreasing depletion layer width opposes the exponential fall of in tunnel current with increasing tip sample separation, hence reducing the fall off in current with distance and resulting in a much lower barrier height measurement. This explains the very slow fall off of current with distance observed for the passivated surface. The effect of tip induced band bending on the oxidised surface is much less because the surface Fermi level is effectively pinned by the surface states, thus the measured barrier height is greater than that for the unpinned surface. (I-S) spectroscopic plots clearly display this difference in the response of the surface band bending to the proximity of the tip.

5.8 Conclusion

We have reported spectroscopic results carried out in air on passivated and unpassivated InP surfaces. The chemical species residing at the surface of both the native oxide and sulphur passivated sample was investigated using XPS. The results indicated that the passivating procedure removed a significant portion of the surface contaminants terminating the surface with a thin sulphur layer. The STM images of the untreated surface displayed a larger degree of surface roughness compared with images of the sulphur passivated surfaces. This roughness is a feature of oxidised surfaces.

The (I-V) spectroscopic results are similar to those reported for similarly treated GaAs surfaces. However, performing I-V spectroscopy was shown to “*damage*” the surface. The results of the (I-S) spectroscopic study show that tip-induced band bending causes considerable lowering of apparent barrier height measurements for unpinned semiconductor surfaces, while for pinned surfaces the effect is greatly reduced. This results in significant differences in the (I-S) spectroscopic plots for the two surfaces. Therefore, while the (I-V) spectroscopic plots display characteristic differences for the differently treated surfaces, the (I-S) spectroscopy displays a quantitative difference between the passivated and unpassivated surfaces, plus unlike the I-V technique, the I-S spectroscopic technique, under the conditions used here, does not physically alter the surface.

Further STS studies germanium surfaces are presented in the final chapter to assess the extent to which this spectroscopic technique can be used to provide some quantification of semiconductor passivation. Also it could prove useful to monitor the

variation in the barrier height with time and the oxide regrowth experienced under ambient conditions

References

- 1 E H Rhoderick and R H Williams, Metal-Semiconductor Contacts, Oxford University Press
- 2 J Bardeen, Phys Rev 71 (1947) 717
- 3 C J Sandroff, R N Nottenburg, J C Bischoff, R Bhat, Appl Phys Lett 51(1987) 33
- 4 R Iyer, R R Chang, D Lile, Appl Phys Lett 53 (1988)134
- 5 J S Ha, S-J Park, S-B Kim and E-H Lee, J Vac Sci Technol A13(3) (1995) 646
- 6 S Nozaki, S Tamura, K Takahashi, J Vac Sci Technol B13(2) (1995) 297
- 7 R Richter and H L Hartnegal, J Electrochem Soc , 127(9) (1990) 2879
- 8 J A Dagata, W Tseng, J Bennett, J Schneir and H H Haray, Appl Phys Lett 59(25) (1991) 3288
- 9 J A Dagata, J Schneir, H H Haray, J Bennett and W Tseng, J Vac Sci Technol B9 (1991) 1384
- 10 J A Dagata, W Tseng, J Bennett, E A Dobisz, J Schneir and H H Haray, J Vac Sci Technol A10 (1992) 2105
- 11 P Moriarty, B Murphy and G Hughes, J Vac Sci Technol A11(4) (1993) 1099
- 12 K Kurihara, Y Miyamoto and K Furuya, Jpn J Appl Phys 32 (1993) L444
- 13 R M Silver, J A Dagata and W Tseng J Appl Phys 76(9) (1994) 5122
- 14 Y Tao, A Yelon, E Sacher, Z H Lu, J Graham , Appl Phys Lett 60(21) (1992) 2669
- 15 C E J Mitchel, J G Hill, A B McLean, Z H Lu , Progress in Surface Science , 50 (1-4) (1995) pp 325-334
- 16 F Maeda , Y Wantanabe , M Oshima , Appl Phys Lett 63(3) (1993) 298
- 17 J A Strocio, R M Fenster , J Vac Sci Technol B 6(4) (1988) 147

18 M Wiemer, J Kramar, J D Baldeschwieler, Phys Rev B, 39(8) (1989) 5572

Chapter 6 : STM/S of Germanium

6.1 Introduction

A major technological drawback to the utilisation of germanium in mainstream device fabrication has been the difficulty in growing on it an insulating oxide comparable to SiO_2 in silicon technology. Indeed, while the oxidation of silicon has been extensively investigated by a wide range of techniques, there are relatively few photoemission studies of germanium oxidation [1-5]. The oxidation characteristics of Ge is seen to be significantly different from Si despite their identical bulk structures and that both elements belong to the same group in the periodic table. From a technological viewpoint, the fact that Ge has a narrower bandgap than Si and has high hole mobility makes it a potential candidate for high performance device applications [6]. In addition, the increase in the number of research investigations of Ge/Si alloy materials necessitates an understanding of the oxidation of these materials, a process which is critical in silicon device fabrication. In addition, there have been even fewer papers [7-9] which have addressed the important process of native oxide removal which is a necessary preparation step to heterostructure growth. It is well known in the literature that HF-based treatments of the low index faces of silicon result in the removal of the native oxides and the termination of the surface dangling bonds with hydrogen. These hydrogen passivated surfaces are resistant to ambient oxidation. An effective HF-based treatment of the Ge(111) surface recently proposed by Deegan et al [9], was shown to remove native oxide from the surface and inhibited the oxide regrowth over an extended period of time. In this chapter the results of a scanning tunnelling microscopy /spectroscopy study of the native oxide and HF etched Ge(111) surface was undertaken to gain further insight into the passivating effects of the HF etch.

6.2 Experimental.

The wafers used in this study were commercially available p-type Ge(111) crystals. The resistivity quoted for the samples was $0.3 \Omega\text{cm}$.

The procedure used to etch the Ge samples was the same as that used by Deegan et al [9]. The sample was first washed in running DI water for 20 seconds. The sample

was then dipped in a 50% HF solution for 10 seconds and followed by a rinse of the sample in running DI water for 20 seconds. The HF etch and water rinse was repeated a total of 5 times. Prior to this the samples were dried in N₂ gas. This procedure was shown [9] to remove the native oxide from the Ge(111) surface and delay oxide regrowth as mentioned in the introduction.

Images of the native oxide and HF etched surfaces were taken under ambient conditions at room temperature with a sample bias voltage of -2V and a setpoint current of 1nA. The images were taken in constant height mode with a scan rate of 3→4 Hz. Stable images of the HF etched surfaces were obtained within half an hour of starting, while for the native oxide surface the STM often had to be left scanning for several hours before the scans stabilised and became repeatable.

All I-V spectroscopy was performed at a setpoint voltage of -1.2 mV and with a tunnel current of 1nA. The I-S measurements were performed at a range of setpoint voltages from -2V to -1V, always at a tunnel current of 1nA.

6.3 STM images of Ge.

Fig 6.1 shows typical images of the native oxide and HF etched surfaces. The r.m.s. roughness of the native oxide surface was 1.43nm, while the r.m.s. roughness of the HF etched surface was only 0.33nm. It is significant that the pattern observed, of the rough native oxide surface and smooth surface of the etched sample, is identical to the case for the native oxide and passivated InP surfaces. This picture also agrees with the findings of Horn et al [10]. This group attributed the drop in intensity of the specular Reflection High Energy Electron Diffraction (RHEED) spots to an increase in the surface roughness, as the clean Ge(001) surface was exposed to both molecular oxygen and carbon monoxide.

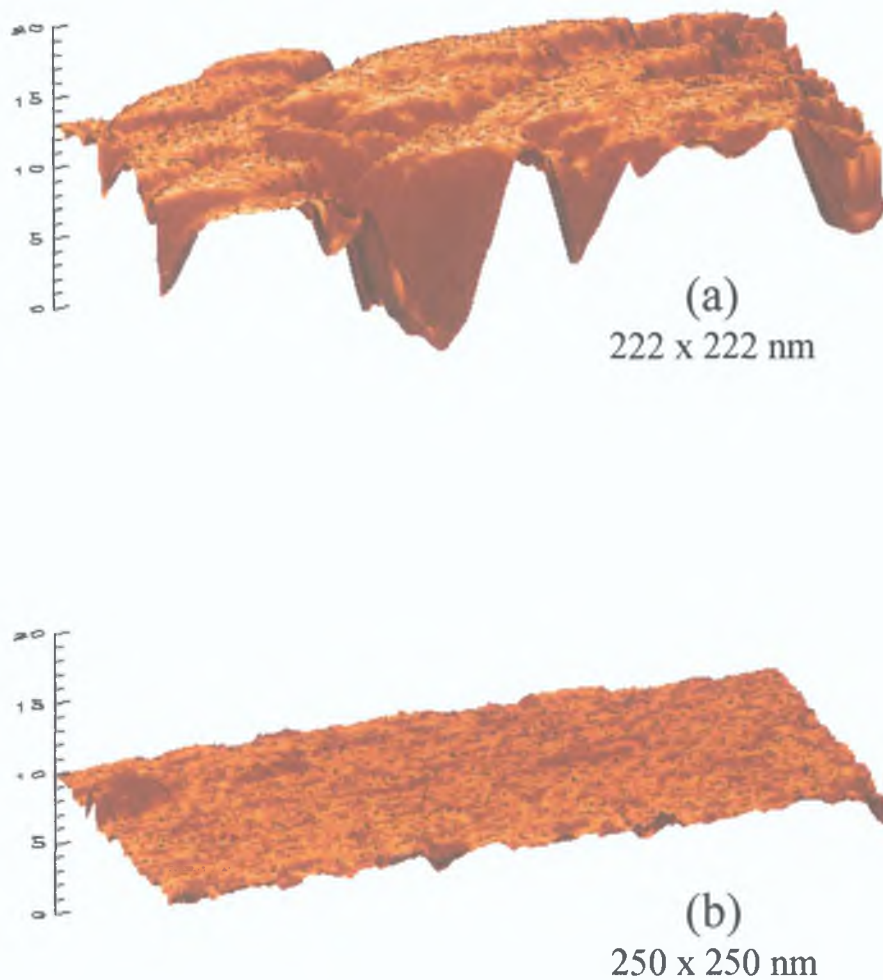


Fig 6.1 Surfaces plots of STM images of (a) the native oxide and (b) HF etched Ge(111) surfaces. Vertical scale is in nm.

6.4 Scanning Tunnelling Spectroscopy of Ge.

6.4.1 I-V Spectroscopy.

There is no reported work in the literature on I-V spectroscopic work on oxygen terminated Ge under either ambient or UHV conditions. In Fig 6.2 we see that the band gap measured for the native oxide and HF etched is quite similar, 0.6 eV for the native oxide sample and 0.7 eV for the HF etched surface.

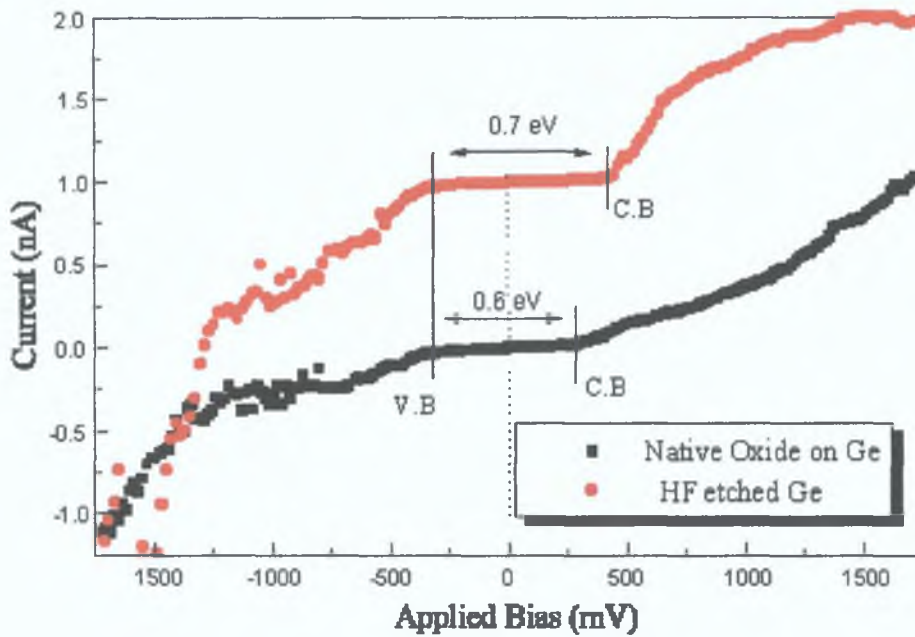


Fig 6.2 I-V spectroscopic plots for the native oxide and HF etched Ge(111) surface.

These values are close to the value of the bulk Ge band gap [11] at room temperature which is 0.67 eV. Fenstra [12] also measured a bandgap of 0.67 eV for a clean Ge(111) surface using I-V spectroscopy under UHV conditions. The fact that the Fermi level (as indicated by the dashed line in Fig 6.2) is slightly closer to the valence band edge (V.B.) than the conduction band edge (C.B.) suggests that the surface is p-type for the HF etched surface. However, this would appear to suggest that for the native oxide surface the Fermi level is pinned midgap.

Fig 6.3 shows the same data as in Fig 6.2 plotted in log form. This shows that there is tunnelling even at low biases in both cases. This can be explained by the fact that there will be a contribution to the tunnel current from surface states known to exist within the band gap [12,13] and also at room temperature there will be some conduction band states occupied due to thermal excitation across the relatively small band gap. The reduced tunnel current at low positive bias (0 → 500 mV) for the HF etched surface may indicate that the treatment results in a reduction of the surface state density between the Fermi level and the conduction band minimum.

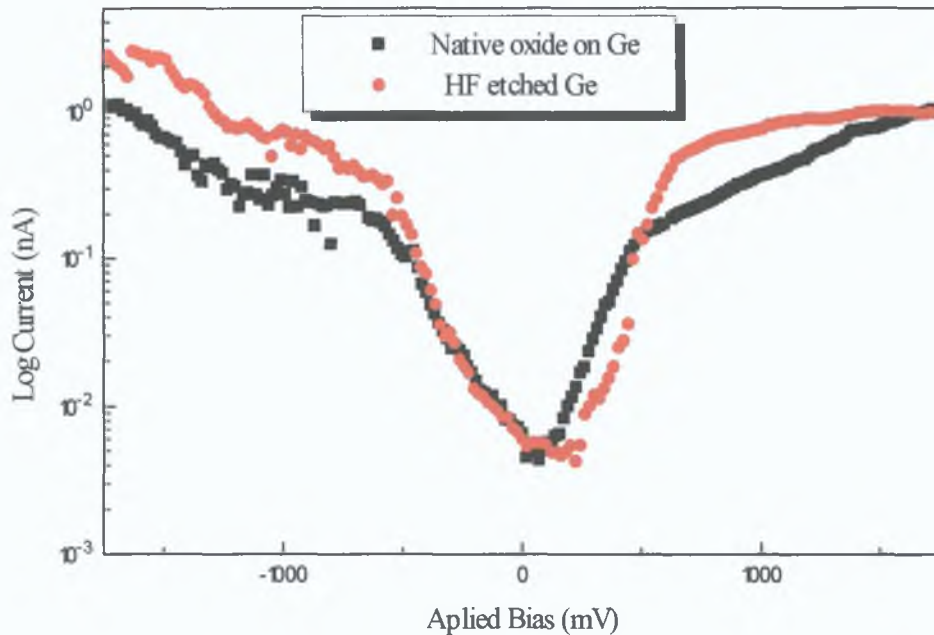
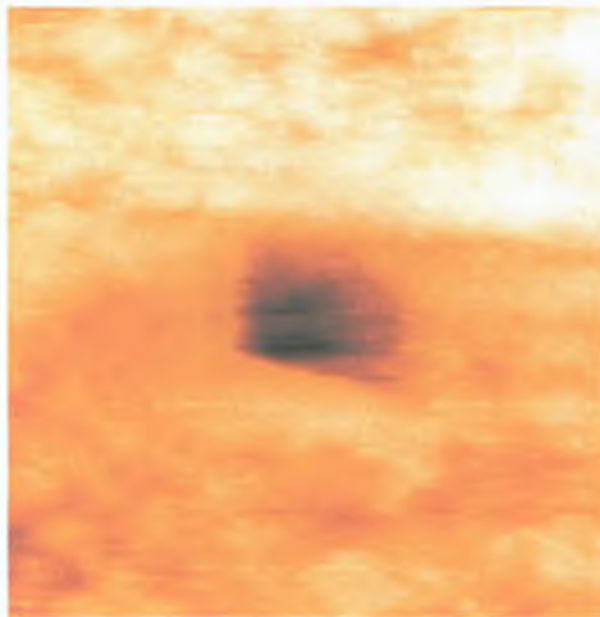
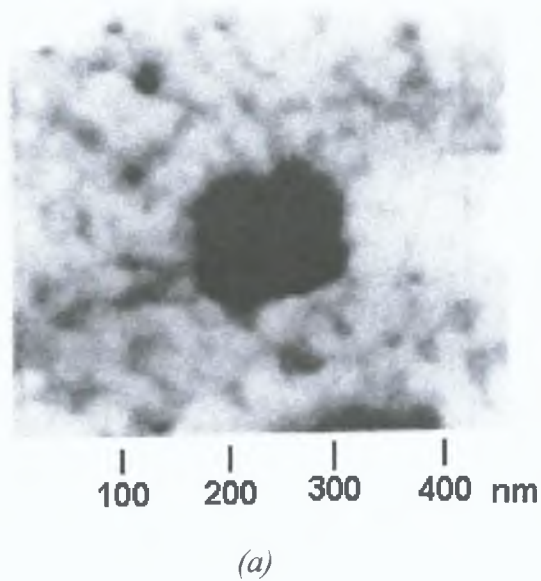


Fig 6.3 I-V plots in log form for the native oxide and HF etched Ge(111) surfaces.

The process of performing I-V spectroscopy on the HF etched Ge(111) surface, locally damaged the surface, as was the case with the sulphur passivated InP surfaces. The damage to the native oxide Ge(111) surface prior to performing I-V spectroscopy was not as pronounced as for the HF etched surface, but noticeable none the less. It was discovered that performing I-S spectroscopy at positive setpoint voltages damaged the surface in a similar manner. This may be linked with the use of positive sample biases (+1.7→ +3.5) by Dagata et al [14] to induce oxide lines on hydrogen terminated Si under ambient conditions. Fig 6.4(a) shows an oxide induced square on the H terminated Si(111) surface observed by Dagata et al [14] and for comparison a similar feature on the HF etched Ge(111) surface produced as a result of I-V spectroscopic measurements on this surface is shown in Fig 6.4(b). For hydrogen terminated Si surface the modification is seen to be due to the desorption of the hydrogen terminating layer and the incorporation of molecular oxygen into the substrate [14-16].



(b) 100 x 100 nm

Fig 6.4 Shows damage induced by (a) imaging the H:Si(111) surface at +3.5V (after Ref. [14]) and (b) performing I-V spectroscopy on the HF etched Ge(111) surface.

6.4.2 I-S Spectroscopy.

Fig 6.5 shows apparent barrier height measurements on the native oxide and HF etched Ge(111) surfaces taken at a range of negative setpoint voltages. Measurements could not be made at positive setpoint voltages because the damage induced on the

surface resulted in the tip crashing or at best spurious data. The average barrier height for the native oxide surface was $\phi_b = 0.7 \pm 0.17$ eV, while for the HF etched surface the average was $\phi_b = 0.067 \pm 0.045$. The value for the barrier height on the native oxide surface is over twice that of

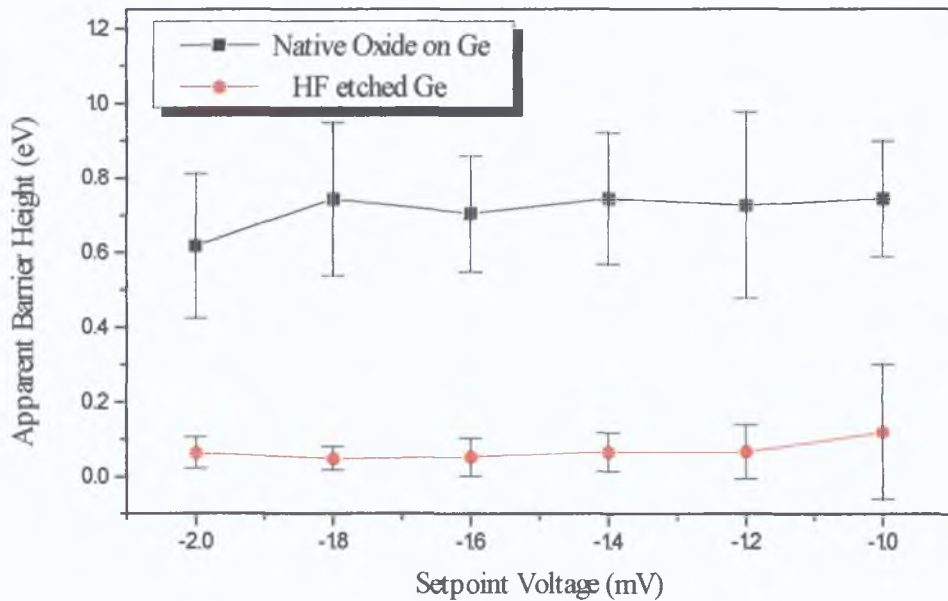


Fig 6.5 Variation in measured apparent barrier height for the native oxide and HF etched Ge(111) surface at different setpoint voltages.

the native oxide of the InP surface, whereas the value for the HF etched Ge surface is very close to that obtained for the passivated InP surface. The most significant factor is that the trend in the barrier height measurements from the native oxide to the etched/passivated surface for both InP and Ge is the same. Following the model used to explain the lower barrier height on the passivated InP surface, this would seem to suggest that the HF etch used unpins the surface Fermi level.

6.5 Conclusions.

In this chapter we have extended the understanding of the spectroscopic techniques which have been developed in the previous two chapters to study an etch of the Ge(111) surface, upon which there has been little previous work. This helps to show the potential of scanning tunnelling spectroscopic work under ambient conditions.

The data provides further evidence indicating that the HF etch of the Ge(111) surface using the method proposed by Deegan et al [9] provides a method of passivating the Ge surface and perhaps unpinning of surface Fermi level.

It is still not clear whether the HF etch leads to a hydrogen termination of the Ge(111) surface as is seen for similar etches of the Si(111) surface. However it has been shown in this chapter that the HF etched Ge surface described here displays similar characteristics to hydrogen terminated Si. This can be seen from the way the etched Ge surface can be perturbed by imaging or performing spectroscopy at positive sample biases, in a manner almost identically to observations on hydrogen terminated Si(111)[14]. Further studies of the etch procedure are necessary to gain the required insight into the surface chemistry and the extent of the passivation of the Ge(111) surface.

References.

- [1] J.E.Rowe, Appl. Phys. Letts. 25(10) (1974) 576.
- [2] D.Schmeisser, R.D.Schnell, A.Bogen, F.J.Himpsel, D.Rieger, G.Landgren and J.F.Morar, Surf. Sci. 172 (1986) 455-465.
- [3] C.M.Garner, I.Lindau, J.N.Millar, P.Pianetta and W.E.Spicer, J. Vac.Sci.Technol 14 (1977) 372.
- [4] K. Prabhakaran, T.Ogino, Surf. Sci. (1995) 263-271.
- [5] Y. Wei, J.L.Sullivan and S.O.Said, Vacuum 45(5) (1994) 597.
- [6] S.M.Sze, Physics of Semiconductor devices (Wiley, New York, 1981).
- [7] X.J.Zhang, G.Xue, A.Agarwai, R.Tsu, M.A.Hasan, J.E.Greene and A.Rockett, J. Vac.Sci.Technol. A11 (1993) 2553.
- [8] K. Prabhakaran, T.Ogino, R.Hull, J.C.Bean and L.J.Peticolas, Surf. Sci. 316 (1994) L1031-L1033.
- [9] T. Deegan, G. Hughes, (Accepted for publication) Appl. Surf. Sci., Proceedings of the 6th International Conference on the formation of semiconductor interfaces.

- [10] K M Horn, E Chason, J Y Tsao, J A Floro, S T Picarux, *Surface Sci*, 320 (1994) 174
- [11] N W Ashcroft, N D Mermin, *Solid State Physics*, (CBS Publishing Asia Ltd , Hong Kong, 1987) , p 566
- [12] R M Fenstra, *Phys Rev B*, 44(24) (1991) 13791
- [13] E H Rhoderick, R H Williams, *Metal-Semiconductor Contacts*, (Clarendon Press, Oxford, 1988)
- [14] J A Dagata, J Schmer, H H Harary, C J Evans, M T Posteck, J Bennett, *Appl Phys Lett* , 56(20) (1990) 2001
- [15] E S Snow, P M Campbell, P J McMarr, *Appl Phys Lett* , 63 (1993) 749
- [16] J W Lyding, T C Chen, J S hubacek, J R Tucker, G C Ablen, *Appl Phys Lett* 64 (1994) 2010

Chapter 7 : Conclusions.

7.1 Summary of Metrological work.

In this thesis a thorough investigation was carried out to establish the metrological capabilities of the Nanoscope II air STM. The study incorporated a comparison of measurements made using two different tip materials, tungsten (W) and platinum Iridium (PtIr). The tip shape was found to play an important role in the measurement process and in particular, the PtIr tips used in this study were shown to be more suitable for imaging the smaller features which were of the order of $1\mu\text{m}$. For features greater than $5\mu\text{m}$ there was little difference between the accuracy of measurements taken using either tip type. Another noteworthy point was the difference in the measured values of the same pitch length, taken using the different tips on the same features.

A method of taking measurements from stored STM images, termed profile differentiation, was developed. The repeatability and accuracy of the Nanoscope II was investigated using this method. It was established that for large features (in this case a $20\mu\text{m}$ pitch grid) a repeatability of better than 1% was achievable using both tip types. For the smaller $3\mu\text{m}$ pitch grid there was almost an insignificant difference between repeated measurements taken using a PtIr tip. The instrument error and the measurement uncertainty were quantified (see Table 3.10). The instrument error was shown to differ depending on the tip material used, which shows the somewhat unpredictable nature of the STM.

Although the Nanoscope II air STM was only purchased in 1991, 6 years ago the technology underlying the technique has developed rapidly and some of the problems considered in this project have been addressed by STM manufacturers and specific STMs have been built geared toward target applications such as metrology. One example of this is the Dimension 5000 Scanning Probe Microscope also available from Digital Instruments, CA which is designed specifically for metrological applications. However, it is hoped this study has demonstrated the sort of difficulties the STM can present as a metrological instrument and that it may provide a platform or guide for evaluating the true metrological capabilities of these newer STMs.

7.2 Conclusions of STS work

In this study we set out to obtain meaningful results from scanning tunnelling spectroscopic measurements and in particular from the I-S technique. The I-S technique has received little attention due mainly to the lack of understanding and confusion surrounding measurements made using the technique.

I-S spectroscopic measurements of the Au(111) yielded a value for ϕ_b of 1.42 eV in air. This value is lower than the theory predicts[1] for a metal-insulator-metal tunnel gap. However, this low value of ϕ_b can be accounted for in the light of similar low ϕ_b measurements made in liquid environments [2-4]. The measured ϕ_b what was deemed to be a reasonable value for the apparent barrier height in air and thus established the foundation for the application scanning tunnelling spectroscopy study of semiconductor surfaces in ambient environments.

The first semiconductor studied was the InP(100) surface and sulphur passivation of that surface. InP has received considerable interest in recent times due to its technological importance for high speed devices and long wavelength optical circuitry. There is also a considerable amount of information on sulphur passivation of the InP surface in the literature, so this surface was considered suitable for an initial STS study of semiconductor surfaces in air. Apparent barrier height measurements of the native oxide InP surface gave a value of 0.3 eV, while the sulphur passivated surface yielded a value of $\phi_b = 0.05\text{eV}$ an order of magnitude lower than that for the unpassivated surface. The lower value for ϕ_b on the passivated surface was explained using the model proposed by Weimer et al [5]. This model states that for an unpinned semiconductor surface that the tip induces band bending therefore increasing the depletion layer at the surface. As the tip is withdrawn from the surface in I-S spectroscopy the effect of the tip-induced band bending is reduced, thus the surface depletion layer is reduced. This effect counteracts the expected exponential fall off in tunnel current with increasing tip sample separation and effectively lowers the measured apparent barrier height ϕ_b .

The Ge(111) surface was the second subject studied using scanning tunnelling spectroscopy. A recently proposed HF etch of this surface [6] was shown to greatly reduce oxide growth. The measured value of ϕ_b for the native oxide on the Ge surface was 0.7 eV. For the HF etched Ge surface, ϕ_b was measured to be 0.067 eV, an order of magnitude lower than the value for the native oxide surface. This is similar to the measurement trend observed for the native oxide and sulphur passivated InP surface. Thus, assuming the same explanation for the lowering of ϕ_b on the passivated InP surface, it would appear to suggest that the HF etch of the Ge surface used resulted in an unpinning of the surface Fermi level. In summary, the studies of the Ge surfaces appear to provide further evidence that the HF etch proposed by Deegan et al [6] provides a method of passivating the Ge(111) surface.

7.3 Suggestions for future research.

Further studies of native oxide and passivated semiconductor surfaces under different environments, but particularly under UHV conditions could be undertaken to establish if the model used to explain the lower barrier height on passivated surfaces holds true. Further studies of the HF etched Ge surface are required to confirm that the etch provides a passivation of the surface and if so what is the atomic geometry of the passivated surface.

It is hoped that this study has provided further insight into the STS technique and in particular I-S spectroscopy. The I-S spectroscopic technique has received comparatively little attention due to a lack of understanding of the tunnelling process in different environments and the confusing measurements obtained in many circumstances. Yet the technique can aid in understanding of the tunnelling process, which is vital to so many applications of scanning tunnelling microscopy, as well as providing a useful quantitative tool.

References.

- 1 G Binnig, H Rohrer, Ch Gerber, E Wiebel, Appl Phys Lett 40(2) (1982) 178
- 2 J Pan, T W Jing, S M Lindsay, J Phys Chem, 92 (1994) 5563
- 3 J Wiechers, T Twomey, D M Klob, J Electroanal Chem, 248 (1988) 451

- 4 R Christoph, H Siegenthaler, H Roher, H Wiese, *Electrochimica Acta*, 8 (1989) 1011
- 5 18 M Wiemer, J Kramar, J D Baldeschwieler, *Phys Rev B*, 39(8) (1989) 5572
- 6 T Deegan, G Hughes, (Accepted for publication) *Appl Surf Sci*, Proceedings of the 6th International Conference on the formation of semiconductor interfaces

Appendix A : RMS roughness calculation.

The rms roughness of an imaged area is calculated by summing the square of each height (defined by a point in x and y) value $z(x,y)$ in the area. This value is divided by the number of points in the area, then the square root is obtained and this corresponds to the root mean square value, S_q . In equation form this can be written as,

$$S_q = \sqrt{\frac{1}{MN} \sum_{k=0}^{M-1} \sum_{l=0}^{N-1} z^2(x_k, y_l)}$$

where $M \times N$ is the number of points in the area being measured

Appendix B : Refereed Publications.

'Ambient Scanning Tunneling Spectroscopy of the sulphur passivated InP(100) surfaces '

Sean Hearne , Greg Hughes, Appl Surf Sci , Proceedings of the Sixth conference on the formation of semiconductor interfaces, (Accepted for publication)